JOURNAL OF COMPUTATIONAL PHYSICS **115**, 319–338 (1994)

Adaptive Multiresolution Schemes for Shock Computations*

AMI HARTEN

Department of Mathematics UCLA, Los Angeles, California 90024 and School of Mathematical Sciences, Tel Aviv University, Tel Aviv, Israel

Received June 14, 1993; revised May 26, 1994

In this paper we present adaptive multiresolution schemes for the computation of discontinuous solutions of hyperbolic conservation laws. Starting with the given grid, we consider the grid-averages of the numerical solution for a hierarchy of nested grids which is obtained by diadic coarsening, and we compute its equivalent multiresolution representation. This representation of the numerical solution consists of the grid-averages of the coarsest grid and the set of errors in predicting the grid-averages of each level of resolution from the next coarser one; these errors depend on the size of the grid and the local regularity of the solution. At a jump-discontinuity they remain the size of the jump, independent of the level of resolution; this observation enables us to identify the location of discontinuities in the numerical solution. In a region of smoothness, once the numerical solution is resolved to our satisfaction at a certain locality of some grid, then the prediction errors there for this grid and all finer ones are small; this enables us to obtain data compression by setting to zero the terms of the multiresolution representation that fall below a specified tolerance. The numerical flux of the adaptive scheme is taken to be that of a standard centered scheme, unless it corresponds to an identified discontinuity, in which case it is taken to be the flux of an ENO scheme. We use the data compression of the numerical solution in order to reduce the number of numerical flux evaluations as follows: We start with the computation of the exact numerical fluxes at the few grid-points of the coarsest grid, and then we proceed through diadic refinement to the given grid. At each step of refinement we add values for the numerical flux at the new grid-points which are the centers of the coarser cells. Wherever the solution is locally well resolved (i.e., the corresponding prediction error is below the specified tolerance) the costly exact value of the numerical flux function is replaced by an accurate enough approximate value which is obtained by an inexpensive interpolation from the values of the coarser grid.

1. INTRODUCTION

In this paper we describe adaptive multiresolution algorithms and simplified essentially nonoscillatory (ENO) schemes for the numerical solution of the initial value problem for hyperbolic conservation laws in one space dimension

$$w_t + f(w)_x = 0, \quad w(x, 0) = w_0(x). \tag{1.1}$$

* This paper is published posthumously. Ami Harten died suddenly and unexpectedly in mid-July in Tel Aviv.

Here $w(x, t)$ is a vector of q components and we assume that the Jacobian $\partial f/\partial w$ has q real eigenvalues $a_1 \le \cdots \le a_q$ and that the corresponding system of right-eigenvectors $\{r_1, \ldots, r_q\}$ spans $\mathbf{R}^q$. To simplify our presentation let us assume that $w_0(x)$ and, consequently, $w(x, t)$ are periodic with a period 1.

Let $x_j^0 = j \cdot h_0$, $0 \le j \le N_0$, be a uniform partition of $[0, 1]$ into N_0 intervals of size h_0, $N_0 = 2^{n_0}$. We consider the numerical solution of (1.1) by the explicit conservative scheme $\mathbf{E_0}$,

$$v_j^{n+1,0} = v_j^{n,0} - \lambda_0(\bar f_j^0 - \bar f_{j-1}^0) \equiv (\mathbf{E_0} \cdot \mathbf{v^{n,0}})_j, \quad 1 \le j \le N_0, \tag{1.2a}$$

where

$$\bar f_j^0 = \bar f(v_{j-K+1}^{n,0}, \ldots, v_{j+K}^{n,0}) \tag{1.2b}$$

is the numerical flux of the scheme. Here $v_j^{n,0}$ is an approximation to the average of the solution $w(x, t)$ in the cell $[x_{j-1}^0, x_j^0]$ at time $t_n = n\tau$, i.e.,

$$v_j^{n,0} \approx \frac{1}{h_0} \int_{x_{j-1}^0}^{x_j^0} w(x, t_n)\, dx. \tag{1.3}$$

The numerical flux function $\bar f(u_1, \ldots, u_{2K})$ is a function of $2K$ arguments which is consistent with the flux $f(w)$ in (1.1) in the sense that

$$\bar f(u, u, \ldots, u) = f(u). \tag{1.4a}$$

$\bar f_j^0$ in (1.2) is an approximation to the time-average of the flux of the solution $f(w(x, t))$ in $[t_n, t_{n+1}]$ at x_j^0,

$$\bar f_j^0 \approx \frac{1}{\tau} \int_{t_n}^{t_{n+1}} f(w(x_j^0, t))\, dt \tag{1.4b}$$

(see [8] for more details).

Let G^k, $0 \le k \le L$, be a set of nested diadic grids

$$G^k = \{x_j^k\}_{j=0}^{N_k}, \quad x_j^k = j \cdot h_k, h_k = 2^k h_0, N_k = N_0/2^k, \tag{1.5}$$

581/115/2-6

0021-9991/94 $6.00

and consider the corresponding sequences of cell-averages $\bar{u}^k = \{\bar{u}_j^k\}_{j=1}^{N_k}$, *of some function* $u(x)$,

$$\bar{u}_j^k = \frac{1}{h_k}\int_{x_{j-1}^k}^{x_j^k} u(x)\,dx. \tag{1.6a}$$

Clearly,

$$\bar{u}_j^k = \tfrac{1}{2}(\bar{u}_{2j-1}^{k-1} + \bar{u}_{2j}^{k-1}), \quad 1 \le j \le N_k; \tag{1.6b}$$

thus, given $\bar{u}^0$ for the finest grid we obtain $\bar{u}^k$, $1 \le k \le L$ (without any explicit knowledge of $u(x)$) by successive applications of (1.6b). Let $\tilde{u}_{2j-1}^{k-1}$ denote the approximation to $\bar{u}_{2j-1}^{k-1}$ which is obtained from the unique polynomial of degree $2s$ that has averages $\bar{u}_{j+l}^k$, $|l| \le s$, in the corresponding cells of the kth grid,

$$\begin{aligned} &\tilde{u}_{2j-1}^{k-1} = \bar{u}_j^k + \sum_{l=1}^{s} \gamma_l(\bar{u}_{j+l}^k - \bar{u}_{j-l}^k), \\ &\bar{r} = 3 \Rightarrow \quad \gamma_1 = -\tfrac{1}{8} \\ &\bar{r} = 5 \Rightarrow \quad \gamma_1 = -\tfrac{22}{128},\ \gamma_2 = \tfrac{3}{128}, \end{aligned} \tag{1.7a}$$

and let $d_j^k(\bar{u}^0)$ denote the corresponding approximation error,

$$d_j^k(\bar{u}^0) = \bar{u}_{2j-1}^{k-1} - \tilde{u}_{2j-1}^{k-1}; \tag{1.7b}$$

here $\bar{r} = 2s + 1$ is the order of accuracy of the approximation (1.7) (see [6] for more details).

If $u(x)$ at $x = \bar{x}$ has $p - 1$ continuous derivatives and a jump-discontinuity in its pth derivative, then for x_j^k near $\bar{x}$

$$d_j^k(\bar{u}^0) \sim \begin{cases} (h_k)^p[u^{(p)}] & \text{for } 0 \le p \le \bar{r} \\ (h_k)^{\bar{r}}\, u^{(\bar{r})} & \text{for } p > \bar{r}, \end{cases} \tag{1.8a}$$

where $[\ \ ]$ denotes the jump at the discontinuity. It follows therefore that

$$|d_{2j}^{k-1}| \approx 2^{-\bar{p}}|d_j^k| \quad \bar{p} = \min(p, \bar{r}), \tag{1.8b}$$

provided that the kth grid is fine enough for the asymptotics to hold. This shows that away from discontinuities of the function, the coefficients $d_j^k(\bar{u}^0)$ diminish in size as we go to a finer grid with a rate which is determined by the local regularity of the function and the order of accuracy of the approximation. In the neighborhood of a discontinuity of $u(x)$, the coefficients $d_j^k(\bar{u}^0)$ remain the same size, independent of the level of refinement.

In [2] we showed that there is a one-to-one transformation between $\bar{u}^0$ and its multiresolution representation $\bar{u}_M$,

$$\bar{u}_M = (d^1, d^2, \ldots, d^L, \bar{u}^L)^{\mathrm{T}}, \tag{1.9}$$

where $d^k = \{d_j^k\}_{j=1}^{N_k}$, which is given by

$\bar{u}_M = \overline{\mathbf{M}}\bar{\mathbf{u}}^0$ (Encoding),

$$\begin{aligned} &\text{DO for } k = 1, 2, \ldots, L \\ &\bar{u}_j^k = \tfrac{1}{2}(\bar{u}_{2j-1}^{k-1} + \bar{u}_{2j}^{k-1}), \qquad 1 \le j \le N_k, \\ &d_j^k = \bar{u}_{2j-1}^{k-1} - \bar{u}_j^k - \sum_{l=1}^{s} \gamma_l(\bar{u}_{j+l}^k - \bar{u}_{j-l}^k), \quad 1 \le j \le N_k. \end{aligned} \tag{1.10}$$

$\bar{u}^0 = \overline{\mathbf{M}}^{-1}\,\bar{\mathbf{u}}_{\mathbf{M}}$ (Decoding),

$$\begin{aligned} &\text{DO for } k = L, L-1, \ldots, 1 \\ &\text{DO for } j = 1, \ldots, N_k \\ &\Delta = \sum_{l=1}^{s} \gamma_l(\bar{u}_{j+l}^k - \bar{u}_{j-l}^k) + d_j^k \\ &\bar{u}_{2j-1}^{k-1} = \bar{u}_j^k + \Delta,\ \bar{u}_{2j}^{k-1} = \bar{u}_j^k - \Delta. \end{aligned} \tag{1.11}$$

We turn now to discuss data compression of $\bar{u}^0$. Let $\hat{u}_M$,

$$\hat{u}_M = \mathbf{tr}_\varepsilon(\bar{\mathbf{u}}_{\mathbf{M}}) = (\hat{\mathbf{d}}^1, \hat{\mathbf{d}}^2, \ldots, \hat{\mathbf{d}}^L, \bar{\mathbf{u}}^L)^{\mathrm{T}} \tag{1.12a}$$

denote the result of the truncation operation on $\bar{u}_M$,

$$\hat{d}_j^k = \begin{cases} d_j^k & \text{if } |d_j^k| > \varepsilon_k \\ 0 & \text{if } |d_j^k| \le \varepsilon_k, \quad 1 \le j \le N_k,\ 1 \le k \le L, \end{cases} \tag{1.12b}$$

and let $\hat{u}^0$ denote the result of applying the decoding algorithm (1.11) to the truncated data $\hat{u}_M$.

In [6] we show that if ε_k in (1.12b) are

$$\varepsilon_k = \varepsilon/2^k, \quad 1 \le k \le L, \tag{1.12c}$$

then for both the L_∞ and L_1 norms,

$$\|\bar{u}^0 - \hat{u}^0\| = \|\overline{\mathbf{M}}^{-1}\,[\bar{u}_M - \mathbf{tr}_\varepsilon(\bar{\mathbf{u}}_{\mathbf{M}})]\,\| \le \mathbf{C}\cdot\varepsilon, \tag{1.12d}$$

where the constant C is independent of the number of levels L.

Let v_M^m *denote the multiresolution representation* (1.9) *of the* numerical solution $v^{m,0}$ (1.2),

$$v_M^m = \overline{\mathbf{M}}v^{m,0} = \{d^1(v^m), \ldots, d^L(v^m), v^{m,L}\}^{\mathrm{T}}, m = n, n+1, \tag{1.13a}$$

ane let $\mathbf{E}_{\mathbf{M}}$ denote the equivalent multiresolution form of the scheme $\mathbf{E}_0$,

$$v_M^{n+1} = \overline{\mathbf{M}}\,\mathbf{E}_0\cdot(\overline{\mathbf{M}}^{-1}\,\mathbf{v}_{\mathbf{M}}^{\mathbf{n}}) \equiv \mathbf{E}_{\mathbf{M}}\cdot\mathbf{v}_{\mathbf{M}}^{\mathbf{n}}. \tag{1.13b}$$

We introduce data compression into the multiresolution scheme (1.13b) by applying the truncation operator $\mathbf{tr}_\varepsilon$ (1.12) to the numerical solution at the beginning of each time-step

$$v_M^{n+1} = \overline{\mathbf{M}}\,\mathbf{E}_0\cdot[\overline{\mathbf{M}}^{-1}\mathbf{tr}_\varepsilon(\mathbf{v}_{\mathbf{M}}^{\mathbf{n}})] \equiv \mathbf{E}_{\mathbf{M}}^{\varepsilon}\cdot\mathbf{v}_{\mathbf{M}}^{\mathbf{n}}; \tag{1.14}$$

since v_M^{n+1} is about to be truncated at the beginning of the next

time-step, only $d_j^k(v^{n+1})$ which are above the tolerance ε_k need to be computed.

In [6] we show how to use this fact to reduce the number of numerical flux calculations (1.2b) which are needed in order to obtain an $O(\varepsilon)$ approximation to the fine-grid solution (1.2a). For the sake of completeness we present this multiresolution algorithm [6, Appendix B] in Section 2 of the present paper.

Our basic assumption in designing this multiresolution algorithm is that the solution w of the IVP (1.1) is resolved to our satisfaction by the fine-grid numerical solution and that the tolerance ε is taken to be of the order of the local truncation error of the fine-grid scheme in the region of smoothness of w. Under these assumptions the multiresolution algorithm improves the computational efficiency by a factor which is proportional to the rate of data compression of the exact solution w on the finest grid, without changing the quality of the numerical results.

The regularity analysis (1.8) shows that the coefficients $d_j^k(\bar{w})$ diminish in size as we go to finer grids, except in the neighborhood of jump-discontinuities where they remain the size of the jump, independent of the level of refinement. Therefore, under the assumptions above, the regions of the finest grid for which $|d_j^l(\bar{w})| > \varepsilon_l = \varepsilon/2$ mark neighborhoods of computationally significant discontinuities. This observation suggests the possibility of designing adaptive schemes which use the numerical flux of the simplest centered scheme, except where $|d_j^l(v^n)| > \varepsilon_{\text{osc}}$, in which case they switch to a numerical flux of a nonoscillatory scheme. In Section 3 we demonstrate this possibility by using the second-order Lax–Wendroff scheme as the basic scheme and switching to the first-order accurate TVD scheme of Roe, where $|d_j^l(v^n)| > \varepsilon_l$.

In Section 4 we consider the new adaptive scheme which uses the simplest centered scheme and switches to an ENO scheme [8] at discontinuities. Compared to the "global ENO" scheme which uses ENO fluxes everywhere, this can be viewed as a "simplified ENO" scheme which switches to the less expensive centered scheme, once it is safe enough to do so.

In Section 5 we go back to the multiresolution framework and describe the algorithm which likewise uses the centered scheme as the basic approximation and switches to the ENO scheme wherever $|d_j^l(v^n)| > \varepsilon_{\text{osc}}$. This adaptive multiresolution scheme offers the added efficiency of eliminating unnecessary numerical flux computations by interpolating fluxes from the coarsest grid for which the required level of accuracy is first achieved.

In Section 6 we present analysis which shows that $|d_j^l(v^n)|$ in the immediate vicinity of a jump discontinuity is a good measure for the size of spurious oscillations that could be generated by the centered scheme if used there. Thus the proposed adaptive scheme switches to a nonoscillatory scheme wherever the use of the centered scheme would generate spurious oscillations of size ε_{osc} or larger.

To the best of our knowledge, [6] and the present work are the first multiresolution schemes for hyperbolic systems of conservation laws. We refer the reader to the earlier works [10, 11, 1], where multiresolution schemes for the regularized Burgers' equation are derived by a Galerkin-like approach with respect to a wavelet basis. These earlier schemes can be viewed as the multiresolution representation of a fine-grid scheme which is obtained by projecting the PDE on the scaling functions of the finest grid. This fine-grid scheme uses a fixed stencil of points and, therefore, unlike TVD and ENO schemes, it produces spurious oscillations at shocks; we suspect that without some regularization it may actually become unstable at stationary shocks. Our approach is different: We start with *any given* scheme in conservation form for the finest grid, and then apply the discrete multiresolution transform M in (1.10) to obtain its multiresolution representation (which is given in (2.1) of the following section).

We would like to point out that the behavior of the scale coefficients in the wavelet expansion which is used in the above mentioned works is similar to that of d_j^k (1.7b)–(1.8) in our method. We refer the interested reader to Daubechies' pioneering work [3] on orthonormal bases of compactly supported wavelets, and to [5, 7], where we compare the multiresolution representation (1.9)–(1.11) which is based on discretization by cell averages to that which results from Daubechies' wavelets.

The ENO scheme which is described in this paper is a generalization of van Leer's MUSCL scheme [9] and the PPM of Colella and Woodward [2] to higher order of accuracy. We would also like to refer the reader to [4] in which we explore the relation between multiresolution analysis and Godunov-type schemes.

2. MULTIRESOLUTION SCHEMES

In [6] we showed that the multiresolution scheme (1.13) can be expressed by

$$\begin{aligned} &d_j^k(v^{n+1}) = d_j^k(v^n) - \lambda_{k-1} D_j^k(\bar{f}), \quad 1 \le j \le N_k,\ 1 \le k \le L, \\ &v_j^{n+1,L} = v_j^{v,L} - \lambda_L(\bar{f}_j^L - \bar{f}_{j-1}^L), \qquad 1 \le j \le N_L; \end{aligned} \tag{2.1a}$$

here

$$\bar{f}_j^k = \bar{f}_{2^k j}^0 = \bar{f}(v_{2^k j-K+1}^{n,0}, \ldots, v_{2^k j+K}^{n,0}), \quad \lambda_{k-1} = \tau/h_{k-1}, \tag{2.1b}$$

and $D_j^k(\bar{f}^0)$ is the interpolation error in approximating $\bar{f}_{2j-1}^{k-1}$ by the unique polynomial of degree $(2s+1)$ which assumes the values $\bar{f}_{j+l}^k$, $-1-s \le l \le s$ at the corresponding points of the kth grid,

$$\begin{aligned} &D_j^k(\bar{f}) = \bar{f}_{2j-1}^{k-1} - \sum_{l=1}^{s+1} \beta_l(\bar{f}_{j+l-1}^k + \bar{f}_{j-l}^k), \\ &(s=0) \Rightarrow \quad \beta_1 = \tfrac{1}{2} \\ &(s=1) \Rightarrow \quad \beta_1 = \tfrac{9}{16}, \beta = -\tfrac{1}{16} \\ &(s=2) \Rightarrow \quad \beta_1 = \tfrac{150}{256}, \beta = -\tfrac{25}{256}, \beta_3 = \tfrac{3}{256}; \end{aligned} \tag{2.1c}$$

the order of accuracy of this central interpolation is $r = 2s + 2$.

The compressed multiresolution scheme (1.14) can also be expressed by (2.1), except that the numerical fluxes in (2.1b) are computed by

$$\bar{f}_j^k = \bar{f}(\hat{v}^{n,0}_{2^k j-K+1}, \ldots, \hat{v}^{n,0}_{2^k j+K}), \quad \hat{v}^{n,0} = \overline{\mathbf{M}}^{-1}\mathbf{tr}_\varepsilon(\overline{\mathbf{M}}\mathbf{v}^{\mathbf{n,0}}). \quad (2.1\hat{b})$$

We note that if $\bar{f}$ is a Lipschitz continuous function of each of its arguments, then (1.12d) implies that the values in (2.1$\hat{b}$) differ from those of (2.1b) by $O(\varepsilon)$.

Let $\bigcup_k D_\varepsilon(v^n)$ denote the set of indices (j, k) of the significant coefficients $d_j^k(v^n)$ in the solution of the compressed multiresolution scheme (1.14),

$$\mathfrak{D}_\varepsilon(v^n) = \{(j,k) \,|\, |d_j^k(v^n)| > \varepsilon_k\}. \quad (2.2)$$

Since v_M^{n+1} is about to be truncated at the beginning of the next time-step in (1.14), only $d_j^k(v^{n+1})$ which are above tolerance, i.e., with $(j, k) \in \mathfrak{D}_\varepsilon(v^{n+1})$, need to be computed. Knowing $\mathfrak{D}_\varepsilon(v^n)$ we compute $\tilde{\mathfrak{D}}^{n+1}$, an overestimate for $\mathfrak{D}_\varepsilon(v^{n+1})$, by enlarging $\mathfrak{D}_\varepsilon(v^n)$ according to the following two rules: (1) If $(j, k) \in \mathfrak{D}_\varepsilon(v^n)$, then during the time-step (which is restricted by the CFL condition) this information may propagate to the two immediate neighbors; thus $(j \pm 1, k)$, in addition to (j, k), are in $\tilde{\mathfrak{D}}^{n+1}$. (2) If $|d_j^k(v^n)|$ has become large to the extent that $2^{1-\bar{r}}|d_j^k(v^n)|$, which is the estimate (1.8b) (with $\bar{p} = \bar{r} - 1$) for both $|d_{2j-1}^{k-1}(v^n)|$ and $|d_{2j}^{k-1}(v^n)|$, is larger than ε_k, then $(2j - 1, k - 1)$ and $(2j, k - 1)$ are in $\tilde{\mathfrak{D}}^{n+1}$; this is equivalent to local refinement. In [7] we suggested the following algorithm which combines the truncation operation with the calculation of $\tilde{\mathfrak{D}}^{n+1}$:

(i) Set

$$\hat{\imath}(j,k) = 0, \quad 1 \le j \le N_k, 1 \le k \le L.$$

(ii)

$$\begin{cases} \text{DO for } k = 1, \ldots, L \\ \text{DO for } j = 1, \ldots, N_k \\ \quad \text{IF } (|\mathbf{d_j^k(v^n)}| \le \varepsilon_\mathbf{k}) \\ \text{THEN} \\ \quad d_j^k(v^n) = 0 \\ \text{ELSE} \\ \quad \begin{cases} \hat{\imath}(j-l,k) = 1, \text{ for } |l| \le 1 \\ \quad \text{IF } (|\mathbf{d_j^k(v^n)}| \ge \mathbf{2^{\bar{r}-1}}\varepsilon_\mathbf{k} \text{ and } k > 1) \\ \text{THEN} \\ \begin{cases} \hat{\imath}(2j-1,k-1) = 1, \\ \hat{\imath}(2j,k-1) = 1 \end{cases} \end{cases} \end{cases} \quad (2.3)$$

(iii) Define $\tilde{\mathfrak{D}}^{n+1}$ by

$$\tilde{\mathfrak{D}}^{n+1} = \{(j,k) \,|\, \hat{\imath}(j,k) = 1\}. \quad (2.4)$$

Next we observe that if both

$$|d_j^k(v^n)| < \varepsilon_k, \quad |d_j^k(v^{n+1})| < \varepsilon_k, \quad (2.5a)$$

then it follows from (2.1a) and (1.12c) that

$$\lambda_0 |D_j^k(\bar{f})| < \varepsilon. \quad (2.5b)$$

This shows that for $(j, k) \in (\tilde{\mathfrak{D}}^{n+1})^c$, the complement of $\tilde{\mathfrak{D}}^{n+1}$, the numerical flux $\bar{f}_j^{k-1}$ can be interpolated from $\bar{f}^k$ within a prescribed tolerance.

In Appendix B of [6] we used this observation in order to present the multiresolution scheme (1.14) as an operation on the given finest grid, in which the numerical fluxes of the given scheme are computed efficiently within a prescribed tolerance by a combination of direct evaluation and interpolation. Given $v^{n,0}$ we calculate $v^{n+1,0}$ by the following algorithm:

Step (i) Apply data compression and define $\tilde{\mathfrak{D}}^{n+1}$:
Compute
$\hat{v}^{n,0} = \overline{\mathbf{M}}^{-1}\mathbf{tr}_\varepsilon(\overline{\mathbf{M}}\mathbf{v}^{\mathbf{n,0}})$;
Use (2.3) to calculate $\hat{\imath}(j, k)$;
define $\tilde{\mathfrak{D}}^{n+1}$ by (2.4).

Step (ii) Compute approximate $\bar{f}^0$:
Evaluate

$$\bar{f}_j^L = \bar{f}(\hat{v}^{n,0}_{i-K+1}, \ldots, \hat{v}^{n,0}_{i+K}), \quad i = j \cdot 2^L, 1 \le j \le N_L \quad (2.6a)$$

$$\begin{cases} \text{DO for } k = L, L-1, \ldots, 1 \\ \text{DO for } j = 1, \ldots, N_k \\ \bar{f}_{2j}^{k-1} = \bar{f}_j^k \\ \quad \text{IF } (\hat{\imath}(\mathbf{j,k}) = \mathbf{1}) \\ \text{THEN} \\ \quad \bar{f}_{2j-1}^{k-1} = \bar{f}(\hat{v}^{n,0}_{i-K+1}, \ldots, \hat{v}^{n,0}_{i+K}), i = (2j-1) \cdot 2^{k-1} \\ \text{ELSE} \\ \quad \bar{f}_{2j-1}^{k-1} = \sum_{l=1}^{s+1} \beta_l (\bar{f}_{j+l-1}^k + \bar{f}_{j-l}^k) \end{cases} \quad (2.6b)$$

Step (iii) Update $v^{n+1,0}$:

$$v_j^{n+1,0} = \hat{v}_j^{n,0} - \lambda_0(\bar{f}_j^0 - \bar{f}_{j-1}^0), \quad 1 \le j \le N_0. \quad (2.6c)$$

Observe that if we skip part (i) and instead set

$$\hat{\imath}(j,k) = 1, \quad i \le j \le N_k, 1 \le k \le L,$$

then the resulting algorithm is just a rearrangement of the given scheme in which the same numerical fluxes,

$$\bar{f}_j^0 = \bar{f}(v^{n,0}_{j-K+1}, \ldots, v^{n,0}_{j+K}), \quad 1 \le j \le N_0,$$

are computed in a different order, except for the extra (now redundant) IF statement. Therefore we can view algorithm (2.6) as a modified version of the given scheme in which the numerical fluxes are computed in an hierarchical way from coarse to fine, and the modification is that direct evaluation of the numeri-

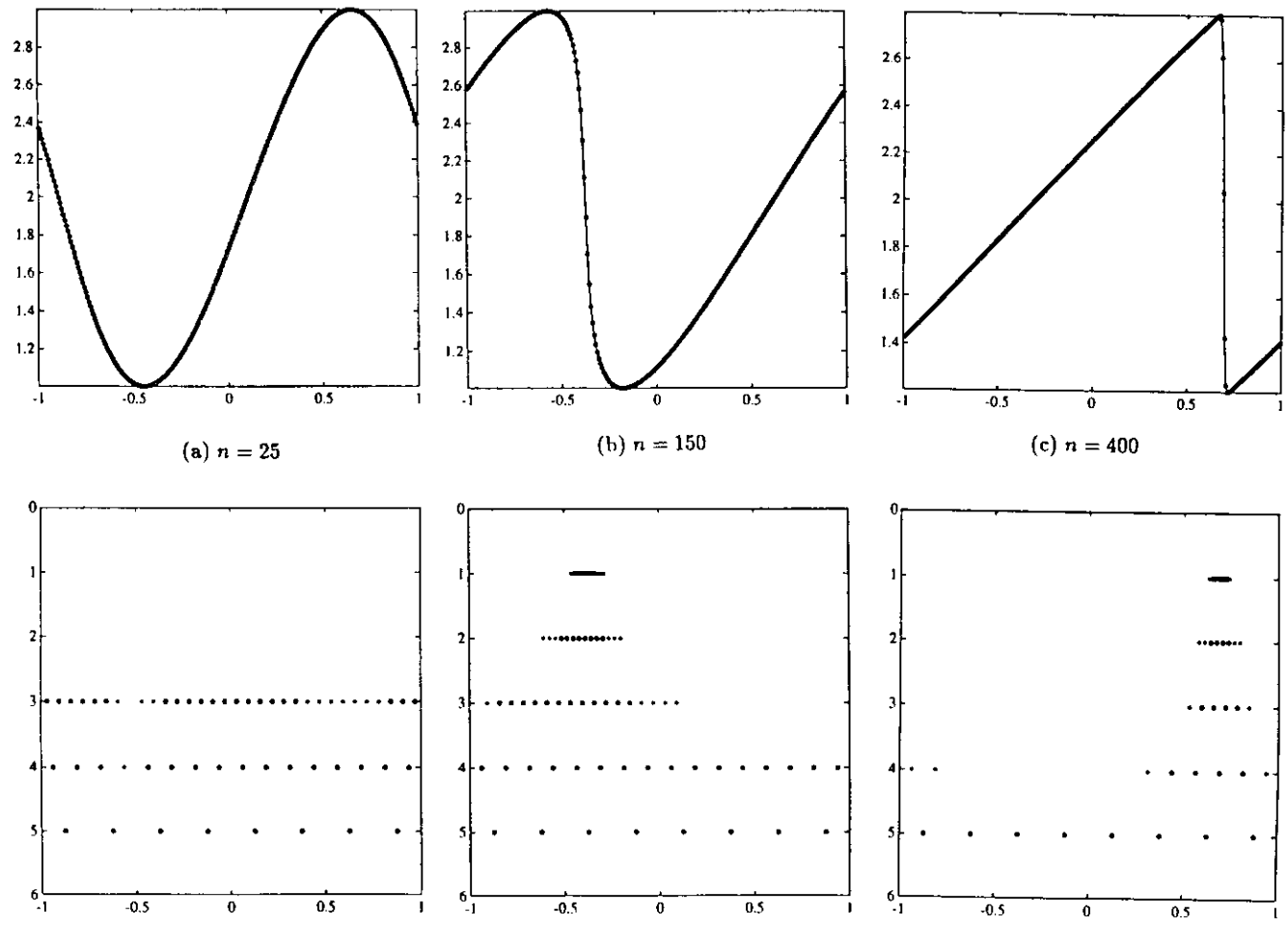

FIG. 1. Multiresolution algorithm for Roe scheme.

cal flux is replaced by interpolation wherever this can be done to a prescribed accuracy. The role of multiresolution in this algorithm is to supply the analysis whether the solution is indeed well resolved at a certain level at a particular locality, so that the representation of the solution can be compressed and the numerical flux can be interpolated from the coarser grid within the specified accuracy.

3. REGULARITY ANALYSIS AND ADAPTIVE SCHEMES

In this section we show how to use the regularity analysis (1.8) in the multiresolution representation in order to switch from a standard high order scheme to a nonoscillatory scheme at shocks.

In Figs. 1 and 2 and the corresponding Tables I and II we present the results of the multiresolution scheme (2.6) for the periodic (IVP),

$$w_t + (w^2/2)_x = 0, \quad w(x, 0) = 2 + \sin \pi x, \quad -1 \le x \le 1. \quad (3.1)$$

In Fig. 1 and Table I we use the numerical flux function (1.2b) of the first-order Roe's scheme,

$$\bar{f}(u_1, u_2) = \tfrac{1}{2}[f(u_1) + f(u_2) - |\bar{a}(u_1, u_2)|(u_2 - u_1)],$$
$$\bar{a}(u_1, u_2) = \begin{cases} [f(u_2) - f(u_1)]/(u_2 - u_1), & u_1 \neq u_2, \\ a(u_1), & u_1 = u_2, \end{cases} \quad (3.2)$$

where $a(u) = f'(u)$.

In Fig. 2 and Table II we use the numerical flux function of the second-order Lax–Wendroff (LW) type scheme,

$$\bar{f}(u_1, u_2) = f\left(\tfrac{1}{2}(u_1 + u_2) - \frac{\lambda_0}{2} a\left(\frac{u_1 + u_2}{2}\right)(u_2 - u_1)\right). \quad (3.3)$$

These calculations were carried out with $N_0 = 256$, CFL $= 0.8$, L $= 5$, $\varepsilon = 10^{-3}$, $\bar{r} = 3$. Each figure consists of three snapshots corresponding to $n = 25, 150, 400$ time-steps which are denoted by a, b, c, respectively.

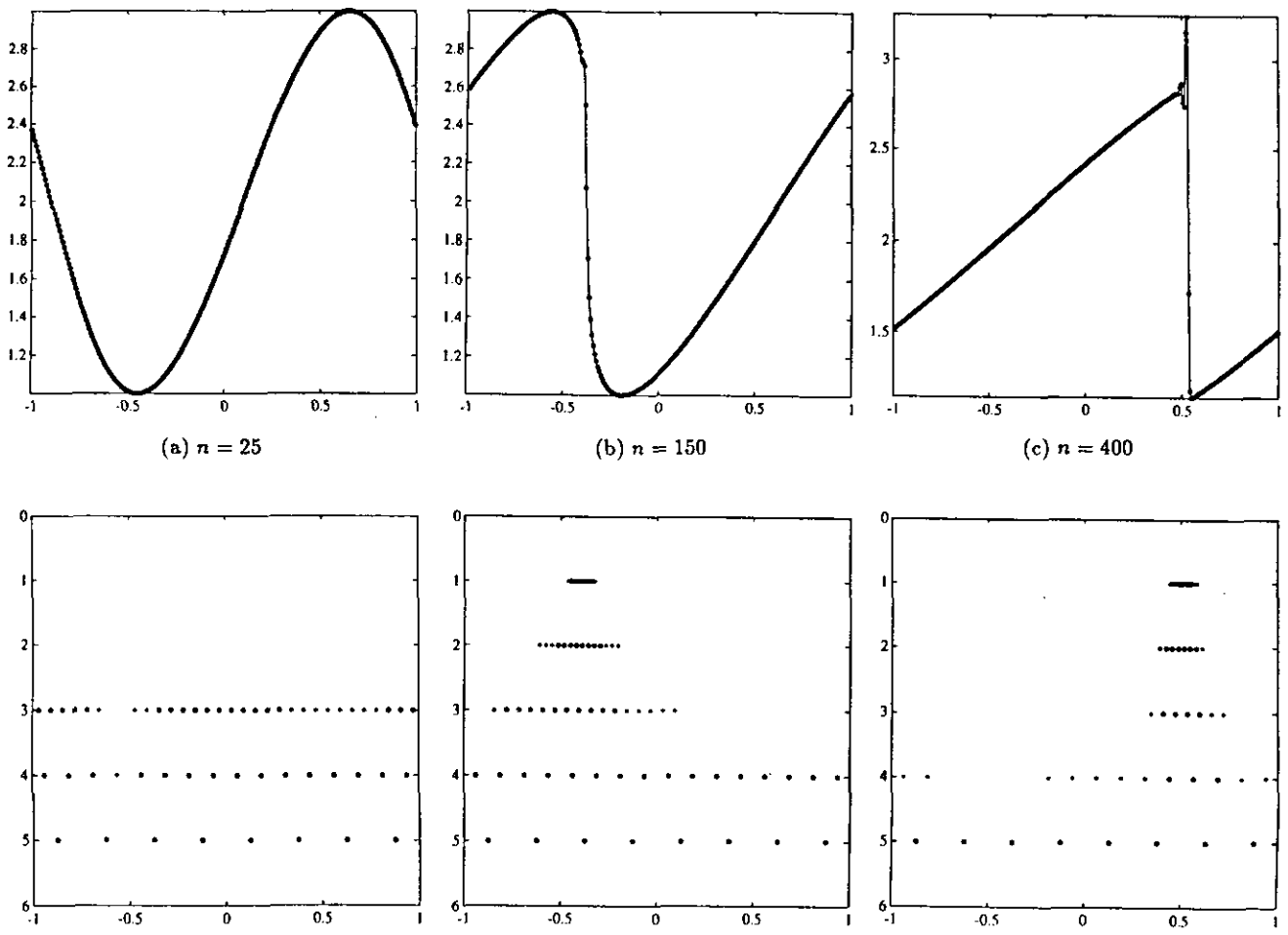

FIG. 2. Multiresolution algorithm for Lax–Wendroff scheme.

In the upper part of each snapshot we compare the solution of the multiresolution scheme (2.5) (circles) with the solution of the fine-grid scheme (1.2) (continuous line) which is computed independently. In the lower part of each snapshot we display $\mathfrak{D}_\varepsilon(v^n)$ (2.2) for the solution of the multiresolution scheme (circles) and its corresponding estimate $\tilde{\mathfrak{D}}^{n+1}$ (2.4) (asterisks). This is done by drawing a symbol at (x_{2j-1}^{k-2l}, k) in the $x - k$ plane for each (j, k) in the set. Because of reduction in the size of the figures the asterisk may look like a dot, and whenever the asterisk is inside the circle we see larger dots.

The solution of (3.1) starts with smooth periodic data with extrema at $x = \pm 0.5$. The segment which has the maximum on its left and the minimum on its right is being steepened into a shock; the segment which is initially between $-0.5 \leq x \leq 0.5$ expands to fill the space in between the shocks, thus forming a decaying N-wave. In Figs. 1a and 2a ($n = 25$, $t = 0.052$)

TABLE I

Multiresolution Algorithm for Roe Scheme

n	Efficiency μ	E_∞	E_1	E_2
25	4.06	3.80×10^{-4}	8.28×10^{-5}	1.15×10^{-4}
150	3.41	4.13×10^{-3}	3.36×10^{-4}	7.79×10^{-4}
400	5.56	3.56×10^{-3}	1.06×10^{-4}	2.98×10^{-4}

Note. $\bar{r} = 3$, $N_0 = 256$, $L = 5$, $\varepsilon = 10^{-3}$.

TABLE II

Multiresolution Algorithm for Lax–Wendroff Scheme

n	Efficiency μ	E_∞	E_1	E_2
25	4.13	3.85×10^{-4}	9.36×10^{-5}	1.25×10^{-4}
150	3.56	8.47×10^{-3}	3.58×10^{-4}	9.10×10^{-4}
400	4.83	7.11×10^{-3}	1.82×10^{-4}	6.31×10^{-4}

Note. $\bar{r} = 3$, $N_0 = 256$, $L = 5$, $\varepsilon = 10^{-3}$.

the solution is still smooth; note that the two figures are almost identical and that the finest levels of resolution 1 and 2 are not used. Comparing Figs. 1b and 2b (and the corresponding entries in Tables I and II) for $n = 150$ ($t = 0.312$), which is about the time of the shock formation, we see that the diagrams for the multiresolution coefficients are almost identical. However, the numerical solution of the two schemes behaves differently. The Roe scheme produces a smooth but smeared transition at the developing shock, while the Lax–Wendroff produces a crisper transition with a kink to the left of the shock; this kink is a result of a postshock overshoot which is compensated by the steep negative slope of the smooth part to its immediate left. Comparing the results at $n = 150$ to those of $n = 25$ we see the addition of finer scales at the shock and the elimination of scale 3 at the rarefaction wave due to its expansion. In Figs. 1c and 2c at $n = 400$ ($t = 0.833$) we see the N-wave structure and observe that $\tilde{\mathfrak{D}}_\varepsilon(v^n)$ has the typical spike at the shock, while the rarefaction, which is almost linear by now, is described by the coarsest level 5. It is interesting to note that despite the *different behaviour at the shock, the multiresolution diagram* for the two schemes is quite similar.

In Tables I and II we show the efficiency factor μ,

$$\mu = \frac{N_0}{|\tilde{\mathfrak{D}}^{n+1}| + N_0/2^L}, \tag{3.4}$$

where $|\tilde{\mathfrak{D}}^{n+1}|$ denotes the number of elements in $\tilde{\mathfrak{D}}^{n+1}$, and the differences E_∞, E_1, and E_2 for $n = 25$, 150, 400 in the corresponding calculations:

$$E_\infty = \max_{1 \le j \le N_0} |e_j|, \tag{3.5a}$$

$$E_p = \left\{ \frac{1}{N_0} \sum_{j=1}^{N_0} |e_j|^p \right\}^{1/p}, \quad p = 1, 2; \tag{3.5b}$$

here e_i denotes the difference at x_i^0 between the solution of the multiresolution algorithm (2.6) and the fine-grid solution (1.2). The L_1-norm seems to be the most appropriate measure for the compression error, and it is interesting to note that it is about the same for the Roe-scheme and the LW-scheme. The maximal pointwise error occurs at the transition of the shock; thus, E_∞ measures the success of the multiresolution algorithm to follow *the details of transition in the fine-grid solution at shocks*, but it has no significance in measuring the accuracy of the multiresolution scheme as an approximation to the exact solution of the IVP (1.1), since the fine-grid scheme itself is not accurate at shocks.

Our basic assumption in designing the multiresolution algorithm (2.6) is that the solution w of the IVP (1.1) is resolved to our satisfaction by the fine-grid numerical solution, and that the tolerance ε is taken to be of the order of the local trunction error of the fine-grid scheme in regions of smoothness of w. Under these assumptions the multiresolution algorithm improves the computational efficiency by a factor which is proportional to the rate of data compression of the exact solution w on the finest grid, without changing the quality of the numerical results.

The regularity analysis (1.8a) shows that $d_j^l(\overline{w})$ is $O([w])$ in the vicinity of a jump-discontinuity in w. Hence if $[w]$ is considerably larger than the variation per cell in regions of smoothness of w, and ε is of the order of the local truncation error there, then we expect $|d_j^l(v^n)|$ to be larger than ε at the discontinuity and its vicinity. For example, in the numerical results of Figs. 1 and 2 we have a shock with a jump of order 1 and $\varepsilon = 10^{-3}$, and indeed we see that the circles of level 1 in the multiresolution diagrams cover a region which is centered at the shock and is proportional to the size of the support of the approximation in (1.7a).

This observation suggests the possibility of designing adaptive schemes which use the regularity analysis in the multiresolution representation of the numerical solution at the beginning *of each time-step in order to select an appropriate numerical* flux function for each location. We demonstrate this possibility in Fig. 3, where we repeat the previous calculations in Figs. 1 and 2 with the following adaptive choice of a numerical flux function $\bar{f}(u_1, u_2)$ in (2.6): At cells $[x_{2j-2}^0, x_{2j}^0]$ for which $|d_j^l(v^n)| > 10^{-3}$ we use the first-order Roe flux (3.2); otherwise we use the second-order LW flux (3.3). In the upper part of Figs. 3a, b, c we present the results of this adaptive multiresolution scheme by circles. In the multiresolution diagram at the bottom of each snapshot we now introduce a new feature: at level 0 we draw an asterisk for each point x_j^0 in which the Roe flux is being used. In Fig. 3a ($n = 25$) the solution is still smooth and the results are identical to those of the Lax–Wendroff scheme in Fig. 2a. In Figs. 3b and c we see no spurious oscillations at the shock and observe that the description of the shock is almost identical to that of the Roe scheme in Figs. 1b and c, respectively. Note that except for a small region around the shock, the computation is done by the LW scheme and that the multiresolution diagrams for the adaptive scheme are similar to the corresponding previous ones.

We note that the switching mechanism which produced the nonoscillatory results in Fig. 3 is based on comparing $|d_j^l(v^n)|$ to ε and had nothing else to do with the multiresolution representation of the solution. In Section 4 we use this observation to introduce a new class of adaptive schemes which are to be *applied in the standard context of a single given grid. In these* adaptive schemes we use the simplest centered scheme as the basic approximation and define a "sensor" η which is identical to $|d_j^l(v^n)|$, and we use the criterion $\eta > \varepsilon_{\text{osc}}$ to switch to a nonoscillatory scheme.

In Section 6 we present an analysis which shows that in the immediate neighborhood of a discontinuity, $\eta = |d_j^l(v^n)|$ measures the spurious oscillations that can be generated per time-step by the corresponding centered scheme. Thus the proposed adaptive scheme switches to a nonoscillatory scheme wherever

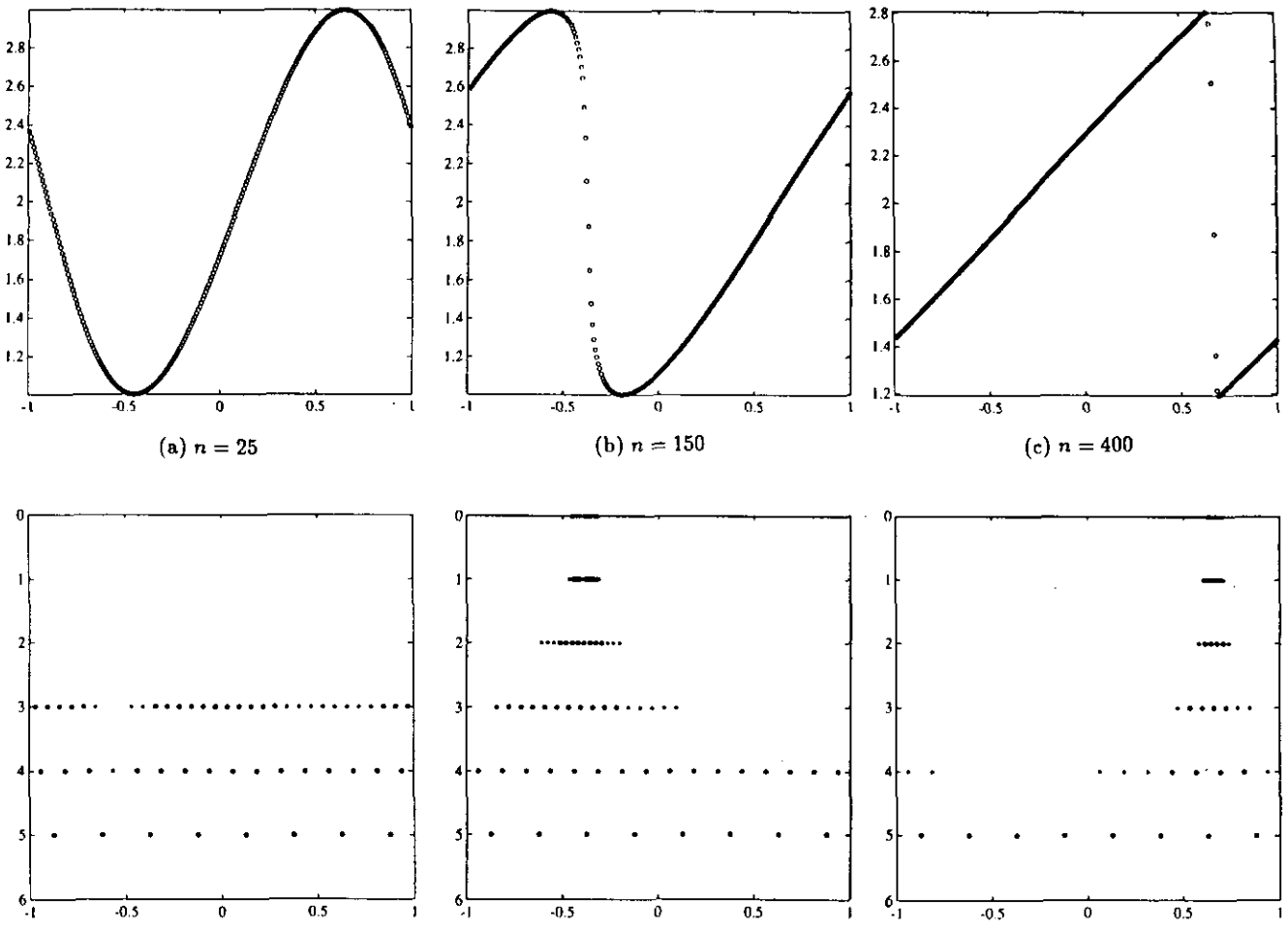

FIG. 3. Multiresolution algorithm for hybrid LW/Roe.

the use of the centered scheme would generate spurious oscillations of size ε_{osc} or larger.

In Section 5 we go back to the multiresolution framework and describe adaptive multiresolution schemes which likewise use the centered scheme as the basic approximation and switch to the ENO scheme wherever $|d_j^l(v^n)| > \varepsilon_{\text{osc}}$. This adaptive multiresolution scheme offers the added efficiency of eliminating unnecessary numerical flux computations by interpolating fluxes from the coarsest grid for which the required level of accuracy is first achieved.

4. SIMPLIFIED ENO SCHEMES

In [8] we introduced a class of ENO schemes that are Godunov-type approximations which use an adaptive selection of stencil in order to avoid generating spurious oscillations at discontinuities. We refer to these schemes as *essentially* nonoscillatory because they still may generate computationally insignificant oscillations on the level of local truncation error in the smooth part of the solution. The major drawback of these ENO schemes is their high computational cost, which results from the need to select a stencil and because, as a Godunov-type scheme, it uses Riemann solvers.

In this section we consider the new adaptive scheme which uses the simplest centered scheme and switches to an ENO scheme at discontinuities. From the point of view of the ENO scheme this adaptive scheme can be considered to be a simplified ENO scheme which switches to a centered scheme once it is safe enough to do so, i.e., wherever the centered scheme will not generate spurious oscillations which are larger than the specified level of tolerance ε_{osc}. Doing so we gain computational efficiency, but now the resulting adaptive scheme may generate "tolerable" spurious oscillations, where the tolerance is specified by the user.

Let $\{x_j\}_{j=0}^N$ be a uniform partition of the given interval in (1.1), where N is an even number: $N = 2N_1$, $N_1 =$ integer, $h = 1/N$. Let $\bar{u}_j$, $1 \le j \le N$, denote the cell-averages of $u(x)$ on the given grid and define

$$\bar{u}_j^l = \tfrac{1}{2}(\bar{u}_{2j-1} + \bar{u}_{2j}), \quad 1 \le j \le N_1 = N/2, \qquad (4.1a)$$

$$\eta([x_{2j-2}, x_{2j}], \bar{u}) = \left| \bar{u}_{2j-1} - \bar{u}_j^l - \sum_{l=1}^{s} \gamma_l (\bar{u}_{j+l}^l - \bar{u}_{j-l}^l) \right|; \qquad (4.1b)$$

thus η above is defined as $|d_j^l(\bar{u})|$ in (1.7) with $k = 1$. Next we define a "flag" vector $\hat{\imath}_0(j)$, $1 \le j \le N$, by the algorithm

(i) *Set*

$$\hat{\imath}_0(j) = 0, \quad 1 \le j \le N,$$

(ii)

$$\begin{cases} \text{DO for } i = 1, \ldots, N_1 \\ \quad \text{IF } (\eta([\mathbf{x_{2j-2}}, \mathbf{x_{2j}}], \bar{\mathbf{u}}) > \varepsilon_{\text{osc}}) \\ \text{THEN} \\ \quad \hat{\imath}_0(j-l) = 1, l = 0, 1, 2 \end{cases} \qquad (4.2a)$$

Using the "flag vector" above we now define the numerical flux of the adaptive scheme as

$$\bar{f}_j(\bar{u}) = \begin{cases} \bar{f}_j^c(\bar{u}), & \text{if } \hat{\imath}_0(j) = 0, \\ \bar{f}_j^s(\bar{u}), & \text{if } \hat{\imath}_0(j) = 1; \end{cases} \qquad (4.2b)$$

here $\bar{f}_j^c$ denotes the numerical flux of a standard centered scheme and $\bar{f}_j^s$ denotes the numerical flux of a scheme which does not generate spurious oscillations at shocks.

The regularity analysis (1.8a) shows that if $u(x)$ has a jump discontinuity of size $[u]$, which is located in (x_{2j_0-2}, x_{2j_0}) then

$$\eta([x_{2j-2}, x_{2j}], \bar{u}) = O([u]) \quad \text{for } |j - j_0| \le s, \qquad (4.3)$$

where $\bar{r} = 2s + 1$ is the support of the approximation in (4.1b). Therefore if ε_{osc} in (4.2a) is such that

$$\varepsilon_{\text{osc}} \ll [u], \qquad (4.4a)$$

then it follows from (4.3) and (4.2b) that

$$\bar{f}_j = \bar{f}_j^s \quad \text{for } (2j_0 - 2) - (\bar{r} - 1) \le j \le 2j_0 + \bar{r} - 1; \qquad (4.4b)$$

i.e., the adaptive scheme (4.2) uses the nonoscillatory flux $\bar{f}_j^s$ in an interval which extends from $(\bar{r} - 1)$ points in front of the shock to $(\bar{r} - 1)$ points past it. Hence the closest to the shock that we use $\bar{f}_j^c$ is $\bar{r}$ points away from it. It follows therefore that if the support of the numerical flux $\bar{f}_j^c$ satisfies

$$K \le \bar{r},$$

where K is defined by (1.2b); then the adaptive scheme (4.2) will not generate spurious oscillations at discontinuities that are large enough to satisfy (4.4a).

The ENO schemes of [8] are Godunov-type schemes for which the numerical flux is an approximation to the integral in (1.4b) by

$$\bar{f}_j^{\text{ENO}} = \sum_m \omega_m \bar{f}^R(\tilde{E}(\nu_m \tau) R_j|_{x_j}, \tilde{E}(\nu_m \tau) R_{j+1}|_{x_j}). \qquad (4.5)$$

In this paper we consider the case of even order of accuracy r and present numerical results for $r = 2$ and $r = 4$. In the following we describe the details of the schemes used in these numerical experiments:

ω_m and ν_m are the coefficients of an appropriate numerical quadrature. For $r = 2$ we use the midpoint rule with

$$r = 2 \Rightarrow \omega_1 = 1, \quad \nu_1 = \tfrac{1}{2}; \qquad (4.6a)$$

for $r = 4$ we use the Gaussian quadrature with

$$r = 4 \Rightarrow \omega_1 = \omega_2 = \frac{1}{2}, \qquad \nu_1 = \frac{1}{2} - \frac{1}{\sqrt{12}}, \quad \nu_2 = \frac{1}{2} + \frac{1}{\sqrt{12}}. \qquad (4.6b)$$

$\bar{f}^R(u_1, u_2)$ denotes the numerical flux of an approximate Riemann solver. In this paper we take it to be the numerical flux (3.2) of the Roe scheme.

$\tilde{E}(\nu_m \tau) u|_{x_j}$ denotes the Taylor expansion around $x = x_j$, $t = 0$ of $E(\nu_m \tau) u$, where $E(t)$ is the exact evolution operator of the IVP (1.1), which is truncated at $O(\tau^r)$, i.e.,

$$\tilde{E}(\nu_m \tau) u|_{x_j} = u|_{x_j} + \nu_m \tau u_t|_{x_j} + \tfrac{1}{2}(\nu_m \tau)^2 u_{tt}|_{x_j} + \cdots + O(\tau^r). \qquad (4.7a)$$

The time-derivatives are computed from the space-derivatives of u via a Cauchy–Kowalewski procedure. For the Burgers equation (3.1) we use for $r = 2$,

$$u_t = -uu_x, \qquad (4.7b)$$

and for $r = 4$ we successively compute

$$\begin{aligned} u_t &= -uu_x \\ u_{xt} &= -(u_x)^2 - uu_{xx} \\ u_{tt} &= u_t u_x - uu_{xt} \\ u_{xxt} &= -3u_x u_{xx} - uu_{xxx} \\ u_{xtt} &= -u_t u_{xx} - 2u_x u_{xt} - uu_{xxt} \\ u_{ttt} &= -u_x u_{tt} - 2u_t u_{xt} - uu_{xtt}. \end{aligned} \qquad (4.7c)$$

Let $P_{j,q}^{r-1}(x; \bar{u})$ denote the unique polynomial of degree $r - 1$ which satisfies

$$\frac{1}{h}\int_{x_{i-1}}^{x_i} P_{j,q}^{r-1}(x;\bar{u}) = \bar{u}_i \quad \text{for } j-q \le i \le j-q+r-1, \tag{4.8}$$

and let $q(j)$ denote a value of q, $0 \le q \le r-1$, such that

$$\left|\frac{d^{r-1}}{dx^{r-1}} P_{j,q(j)}^{r-1}\right| = \min_{0\le q\le r-1}\left|\frac{d^{r-1}}{dx^{r-1}} P_{j,q}^{r-1}\right|. \tag{4.9a}$$

We define R_j in (4.5) by

$$R_j = P_{j,q(j)}^{r-1}(x; v^n). \tag{4.9b}$$

For $r = 2$ we get in (4.9) that $R_i(x; v^n)$ in $[x_{i-1}, x_i]$ is given by

$$R_i = v_i^n + \left(\frac{x - x_{i-1/2}}{h}\right) S_i, \tag{4.10a}$$

$$S_i = \overline{m}(v_i^n - v_{i-1}^n, v_{i+1}^n - v_i^n), \tag{4.10b}$$

where $\overline{m}(x, y)$ is defined by

$$\overline{m}(x,y) = \begin{cases} x & \text{if } |x| \le |y| \\ y & \text{if } |y| < |x|. \end{cases} \tag{4.11}$$

Thus

$$\begin{aligned} R_j|_{x_j} &= v_j^n + \frac{1}{2}S_j \equiv v_{j,L}, \qquad \frac{\partial}{\partial x}R_j|_{x_j} = S_j/h, \\ R_{j+1}|_{x_j} &= v_{j+1} - \frac{1}{2}S_{j+1} \equiv v_{j,R}, \quad \frac{\partial}{\partial x}R_{j+1}|_{x_j} = S_{j+1}/h, \end{aligned} \tag{4.12a}$$

and therefore we get in (4.3)

$$\begin{aligned} \tilde{E}(\tfrac{1}{2}\tau)R_j|_{x_j} &= v_{j,L} - \tfrac{1}{2}\lambda f'(v_{j,L})S_j \\ \tilde{E}(\tfrac{1}{2}\tau)R_{j+1}|_{x_j} &= v_{j,R} - \tfrac{1}{2}\lambda f'(v_{j,R})S_{j+1}. \end{aligned} \tag{4.12b}$$

Hence the second-order ENO scheme in (4.1) is

$$\bar{f}_j^{\mathrm{ENO}} = \bar{f}^{\mathrm{ROE}}(v_{j,L} - \tfrac{1}{2}\lambda f'(v_{j,L})S_j, v_{j,R} - \tfrac{1}{2}\lambda f'(v_{j,R})S_{j+1}), \tag{4.12c}$$

where $\bar{f}^{\mathrm{ROE}}$ is the numerical flux (3.2) of the Roe scheme; in [8] we show that (4.12c) is a TVD scheme.

We turn now to consider a version of the standard centered scheme which is defined by its numerical flux $\bar{f}_j^{\mathrm{CTR}}$ as

$$\bar{f}_j^{\mathrm{CTR}} = \sum_m \omega_m f(\tilde{E}(\nu_m\tau)R^c|_{x_j}); \tag{4.13a}$$

here ω_m, ν_m, and $\tilde{E}$ are as in (4.6)–(4.7), and the reconstruction R^c is (4.8) with a stencil of r cells (r = even) which is symmetric around $x = x_j$, i.e., $q = r/2 - 1$,

$$R^c = P_{j,r-1}^{r-1}(x; v^n). \tag{4.13b}$$

Note that for $r = 2$,

$$\begin{aligned} R^c|_{x_j} &= \frac{1}{2}(v_j^n + v_{j+1}^n), \\ \frac{\partial}{\partial x}R^c|_{x_j} &= \frac{1}{h}(v_{j+1}^n - v_j^n), \end{aligned} \tag{4.14a}$$

$$\tilde{E}\left(\frac{1}{2}\tau\right)R^c|_{x_j} = \frac{1}{2}(v_j^n + v_{j+1}^n) - \frac{1}{2}\lambda f'\left(\frac{v_j^n + v_{j+1}^n}{2}\right)(v_{j+1}^n - v_j^n), \tag{4.14b}$$

$$\bar{f}_j^{\mathrm{CTR}} = f\left(\frac{1}{2}(v_j^n + v_{j+1}^n) - \frac{1}{2}\lambda f'\left(\frac{v_j^n + v_{j+1}^n}{2}\right)(v_{j+1}^n - v_j^n)\right). \tag{4.14c}$$

and thus $\bar{f}_j^{\mathrm{CTR}}$ in (4.14c) coincides with the numerical flux (3.3) of the Lax–Wendroff scheme.

We observe that since $\bar{f}^R(u_1, u_2)$ is a Lipschitz-continuous function which is consistent with $f(u)$ we have

$$\bar{f}^R(u_1, u_2) = f(u) + O(|u - u_1| + |u - u_2|). \tag{4.15a}$$

It follows then from (4.5) and (4.13) that

$$\bar{f}_j^{\mathrm{ENO}} = \bar{f}_j^{\mathrm{CTR}} + O\left(\sum_{l=0}^{r-1}\frac{\tau^l}{(l+1)!}\left\{\left|\frac{\partial^l}{\partial t^l}[E(t)R_j - E(t)R^c]\right| + \left|\frac{\partial^l}{\partial t^l}[E(t)R_{j+1} - E(t)R^c]\right|\right\}\right), \tag{4.15b}$$

where the derivatives in the RHS of (4.15b) are evaluated at $x = x_j$, $t = 0$. If $R^c|_{x_j}$ and its derivatives to order $(r-1)$ there are close to those of R_j and R_{j+1}, then the difference term in the RHS of (4.15b) is small. When the solution $w(x, t)$ of (1.1) is r-times differentiable then

$$\frac{\partial^l}{\partial x^l}P_{j,q}^{r-1}(x;\bar{w}) = \frac{\partial^l}{\partial x^l}w + O(h^{r-l}) \quad \forall 0 \le q \le r-1; \tag{4.15c}$$

in this case each term in the sum in the RHS of (4.11b) is $O(h^r)$.

The evaluation of $\bar{f}_j^{\mathrm{CTR}}$ (4.13) is considerably less expensive than that of $\bar{f}_j^{\mathrm{ENO}}$ (4.5). The analysis of (4.15) shows that $\bar{f}_j^{\mathrm{CTR}}$ can be thought of as a simplification of $\bar{f}_j^{\mathrm{ENO}}$ which is obtained by locally approximating the discontinuous ENO reconstruction

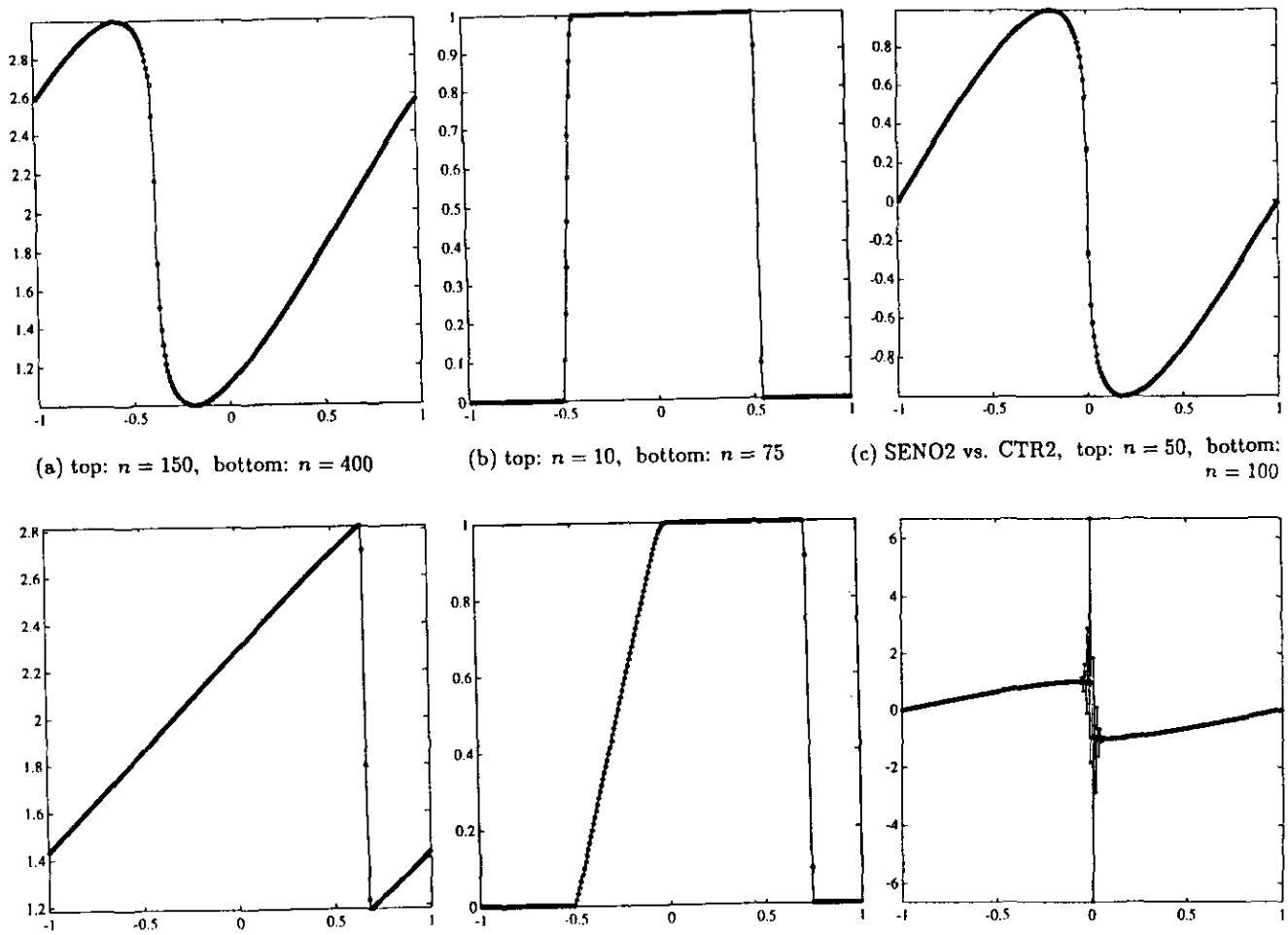

(a) top: $n = 150$, bottom: $n = 400$ (b) top: $n = 10$, bottom: $n = 75$ (c) SENO2 vs. CTR2, top: $n = 50$, bottom: $n = 100$

FIG. 4. Numerical experiments with SENO2.

$$R^{\mathrm{ENO}} = \begin{cases} R_j, & x < x_j, \\ R_{j+1}, & x > x_j, \end{cases}$$

by $R = R^c$ for both sides of $x = x_j$. The centered scheme is not a Godunov-type scheme, but it is linearly L_2-stable and thus can be safely used in regions where the solution is smooth.

We turn now to consider the adaptive scheme (4.2), where $f_j^s = \bar{f}_j^{\mathrm{ENO}}$ and $\bar{f}_j^c = \bar{f}_j^{\mathrm{CTR}}$; i.e.,

$$\bar{f}_j = \begin{cases} \bar{f}_j^{\mathrm{ENO}}, & \text{if } \hat{\imath}_0(j) = 1, \\ \bar{f}_j^{\mathrm{CTR}}, & \text{if } \hat{\imath}_0(j) = 0, \end{cases} \tag{4.16}$$

and denote the second-order scheme by SENO2 and the fourth-order one by SENO4. The scheme (4.16) can be thought of as a simplified ENO scheme in which we replace the ENO numerical flux by the simpler centered one wherever the solution is sufficiently smooth.

In Figs. 4a,b,c and Table III we present results of SENO2 for the Burgers equation with $\bar{r} = 3$ and $\varepsilon_{\mathrm{osc}} = 5 \times 10^{-3}$ in (4.1)–(4.2) for three different sets of initial values which were all performed with $N_0 = 256$ and CFL $= 0.8$; these results are shown by circles. In Fig. 4a we show results for the IVP (3.1) at $n = 150$ (top) and $n = 400$ (bottom) and compare them to those of ENO2, the second-order ENO scheme, which are shown by a continuous line. In Fig. 4b we repeat this comparison for the results of the periodic IVP,

$$\begin{aligned} &w_t + (w^2/2)x = 0, \\ &w(x, 0) = \chi_{[-0.5,0.5]}(x) = \begin{cases} 1, & |x| \le 0.5, \\ 0, & 0.5 < |x| \le 1, \end{cases} \end{aligned} \tag{4.17}$$

at $n = 10$ (top) and $n = 75$ (bottom). In Fig. 4c we show the results for the IVP

$$\begin{aligned} &w_t + (w^2/2)_x = 0, \\ &w(x, 0) = -\sin \pi x, \quad -1 \le x \le 1, \end{aligned} \tag{4.18}$$

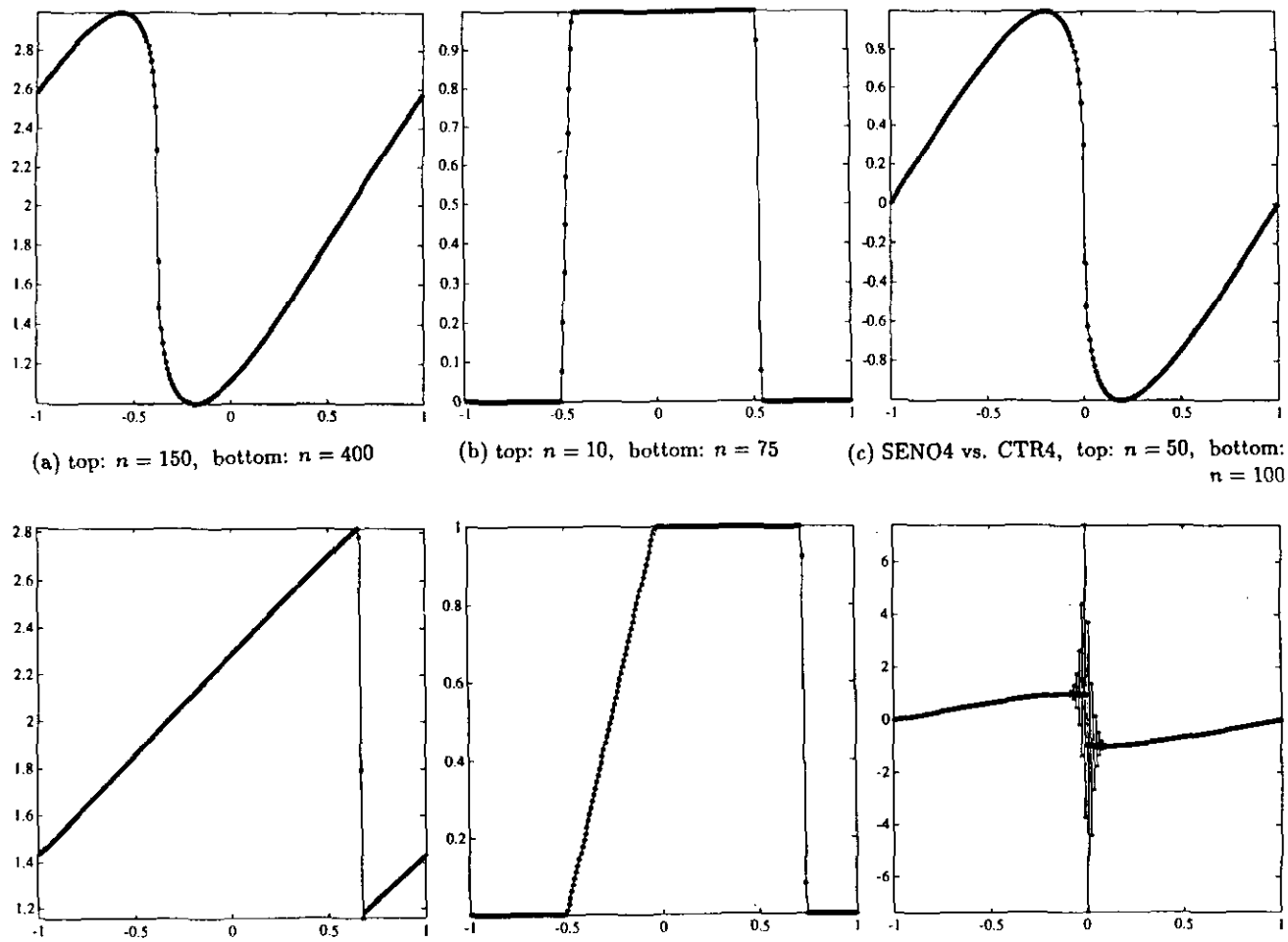

(a) top: $n = 150$, bottom: $n = 400$ (b) top: $n = 10$, bottom: $n = 75$ (c) SENO4 vs. CTR4, top: $n = 50$, bottom: $n = 100$

FIG. 5. Numerical experiments with SENO4.

at $n = 50$ (top) and $n = 100$ (bottom). Here we compare the results of SENO2 (circles) with those of CTR2, the second-order centered scheme in (4.14), which are shown by asterisks connected by a line; this scheme is identical to the LW scheme (3.3).

In Table III we show the number of times that the ENO flux (4.5) was used, and the difference Ep, $p = 1, 2, \infty$ (3.5) between the numerical solutions of SENO2 and ENO2. Here we introduce a new entry E_∞ (smooth) which is calculated by restricting the maximum in (3.5a) to points j for which $\hat{i}_0(j) = 0$ for SENO2.

In Figs. 5a,b,c and Table IV we repeat the calculations of Fig. 4 and Table III for SENO4 with the same $\bar{r} = 3$ and $\varepsilon_{osc} = 5 \times 10^{-3}$ in (4.1)–(4.2) and compare the results of SENO4 to those of the corresponding fourth-order schemes ENO4 (4.5) and CTR4 (4.13).

We make the following observations regarding the numerical experiments in Figs. 4 and 5:

(1) The simplified ENO scheme (SENO) produced nonoscillatory results which are almost identical to those of the corresponding ENO scheme, except that the SENO results are more accurate in regions of smoothness of the solution; this is due to the fact that the centered scheme has a smaller local truncation error and a slower accumulation of error than that of the corresponding ENO scheme.

(2) As predicted by (4.4b) for a shock transition of two cells, SENO with $\bar{r} = 3$ switched to the ENO flux at seven points which are centered around the shock; in other experiments, which are not presented here, we found that SENO with $\bar{r} = 5$ in the same situation uses ENO flux at 11 points, as predicted by (4.4b).

(3) In Figs. 4b and 5b we show results of SENO for a centered rarefaction wave which evolves from an initial discontinuity at $x = -0.5$ and has discontinuous first-derivatives at its endpoints. We find that SENO used eight ENO fluxes altogether at the rarefaction at $n = 10$ and none at $n = 75$. Although the centered scheme generates spurious oscillations at corners, we *cannot see* any in the graphical output for $n = 75$.

(4) It is important to switch to a nonoscillatory scheme at shocks, not only because spurious oscillations are "ugly." As the results in Figs. 4c and 5c show, there are circumstances where these spurious oscillations in the centered scheme

TABLE III

SENO2 for Burgers Equation in Fig. 4

IVP	n	ENO calls	E_∞	E_∞ (smooth)	E_1	E_2
(3.1)	150	9	6.59×10^{-2}	3.79×10^{-3}	8.58×10^{-4}	5.45×10^{-3}
	400	7	5.77×10^{-3}	7.00×10^{-4}	6.28×10^{-5}	3.80×10^{-4}
(4.17)	10	15	0	0	0	0
	50	6	1.03×10^{-3}	1.03×10^{-3}	1.70×10^{-5}	9.65×10^{-5}
(4.18)	50	6	3.31×10^{-2}	3.31×10^{-2}	6.30×10^{-4}	3.61×10^{-3}
	100	5	5.48×10^{-6}	1.49×10^{-6}	1.23×10^{-7}	5.31×10^{-7}

Note. $N_0 = 256$, CFL $= 0.8$, $\bar{r} = 3$, $\varepsilon_{\text{osc}} = 5 \times 10^{-3}$.

can accumulate to the point of instability. The switch to the ENO flux at five points around the stationary shock in the SENO schemes was sufficient to ensure a nonoscillatory solution.

(5) SENO switches between two schemes which have the same order of accuracy. Thus the choice of $\bar{r}$ (say $\bar{r} = 3$ for SENO4) determines the width of the stencil around the discontinuity, where SENO uses the ENO flux, but it has nothing to do with the formal order of accuracy of the adaptive scheme.

5. ADAPTIVE MULTIRESOLUTION SCHEMES

In this section we describe in detail the adaptive multiresolution algorithm which corresponds to the simplified ENO schemes of Section 4. Here we replace $\hat{\imath}_0(j)$ in (4.2) by $\hat{\imath}(j, 0)$ and incorporate its calculation in (2.3). Thus steps (ii) and (iii) (2.6) remain the same, and step (i) is replaced by the following subalgorithm:

(1) Encode: Use (1.10) to compute

$$v_M^n = \overline{\mathbf{M}} v^{n,0} \tag{5.1a}$$

(2) Set

$$\hat{\imath}(j, k) = 0, \quad 1 \le j \le N_k, 0 \le k \le L$$

(3)

$$\begin{cases} \text{DO for } j = 1, \ldots, N_1 \\ \quad \text{IF } (|\mathbf{d}_j^1(\mathbf{v}^n)| > \varepsilon_{\text{osc}}) \\ \text{THEN} \\ \quad \hat{\imath}(2j - l, 0) = 1, l = 0, 1, 2. \\ \text{ELSE} \\ \quad \begin{cases} \quad \text{IF } (|\mathbf{d}_j^1(\mathbf{v}^n)| > \varepsilon_1) \\ \text{THEN} \\ \hat{\imath}(j - l, 1) = 1, l = -1, 0, 1. \\ \text{ELSE} \\ d_j^1(v^n) = 0 \end{cases} \end{cases} \tag{5.1b}$$

(4)

$$\begin{cases} \text{DO for } k = 2, \ldots, L \\ \text{DO for } j = 1, \ldots, N_k \\ \quad \text{IF } (|\mathbf{d}_j^k(\mathbf{v}^n)| \le \varepsilon_k) \\ \text{THEN} \\ \quad d_j^k(v^n) = 0 \\ \text{ELSE} \\ \quad \begin{cases} \hat{\imath}(j - l, k) = 1, l = -1, 0, 1. \\ \quad \text{IF } (|\mathbf{d}_j^k(\mathbf{v}^n)| \ge 2^{i-1}\varepsilon_k) \\ \text{THEN} \\ \quad \hat{\imath}(2j - l, k - 1) = 1, l = 0, 1. \end{cases} \end{cases} \tag{5.1c}$$

(5) Decode: Use (1.11) to compute

$$v^{n,0} = \overline{\mathbf{M}}^{-1} v_M^n. \tag{5.1d}$$

We use the newly defined quantity $\hat{\imath}(j, 0)$ in step (ii) as we did in (4.2b); i.e., we define the numerical flux $\bar{f}_j^0$,

$$\bar{f}_j^0 = \bar{f}(v_{j-K+1}^{n,0}, \ldots, v_{j+K}^{n,0}), \tag{5.2a}$$

by

$$\bar{f}_j^0 = \begin{cases} \bar{f}_j^{\text{CTR}}, & \text{if } \hat{\imath}(j, 0) = 0, \\ \bar{f}_j^{\text{ENO}}, & \text{if } \hat{\imath}(j, 0) = 1. \end{cases} \tag{5.2b}$$

In Figs. 6 and 7 we repeat the calculations of Figs. 1–3 for the second- and fourth-order adaptive multiresolution schemes which are given by (5.1)–(5.2), (2.6) and denoted by MRSENO2 and MRSENO4, respectively. As before, we solve the periodic IVP (3.1) with $N_0 = 256$, CFL $= 0.8$, and $L = 5$ levels of resolution, and we present results for $n = 25$, 150, 400 time-steps which are denoted by parts a, b, c, respectively. In the top part of each of these snapshots we compare the results of the adaptive multiresolution scheme, which are shown by circles, to those of the ENO scheme of the same order

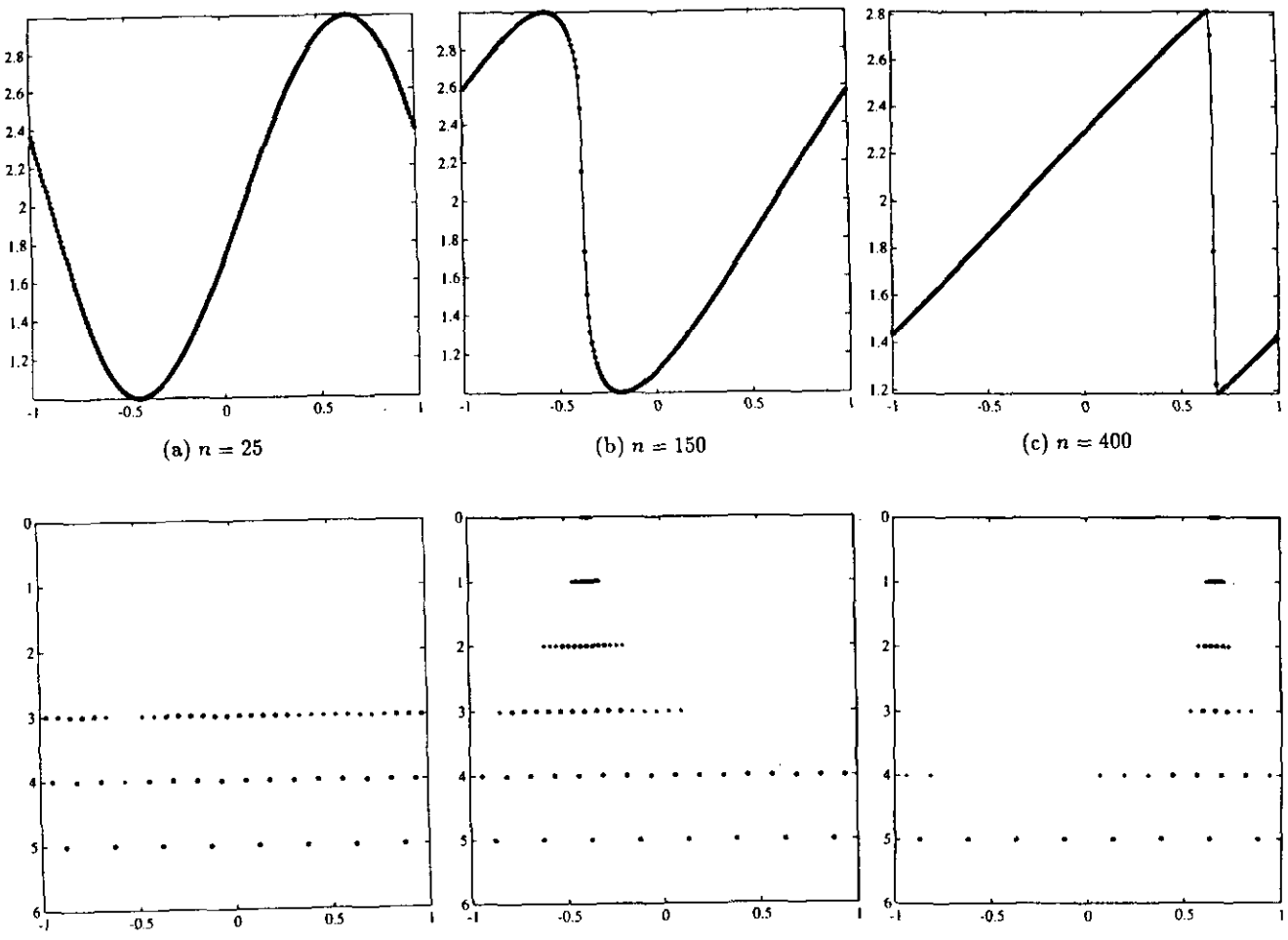

(a) $n = 25$ (b) $n = 150$ (c) $n = 400$

FIG. 6. Second-order adaptive multiresolution scheme (MRSENO2).

(ENO2 and ENO4), which are shown by a continuous line. In the multiresolution diagram at the bottom of each snapshot, we display at level 0 the locations in which the ENO flux was used, by drawing an asterisk at all x_j^0 for which $\hat{i}(j, 0) = 1$. In the corresponding Tables V and VI we show for each snapshot in the figure: the efficiency factor μ (3.4), the number of ENO fluxes vs. that of centered fluxes, and E_p, $p = 1, 2, \infty$ (3.5), and E_∞ (smooth) for the difference between the solution of the adaptive multiresolution scheme and the ENO solution, which are shown in the figures; E_∞ (smooth) is calculated by restricting the maximum in (3.5a) to points j for which $\hat{i}(j, 0) = 0$.

In Fig. 6 we use the second-order MRSENO2 with $\varepsilon = 10^{-3}$, $\bar{r} = 3$, and $\varepsilon_{\text{osc}} = 5 \times 10^{-3}$; note that the last two parameters are the same as in Fig. 4a. In Fig. 7 we use the fourth-order MRSENO4 with $\varepsilon = 10^{-5}$, $\bar{r} = 5$, and $\varepsilon_{\text{osc}} = 5 \times 10^{-3}$. We would like to make the following observations regarding these results:

(1) There are no noticeable spurious oscillations in both cases; the results of the adaptive multiresolution scheme are very close to those of the corresponding ENO scheme.

(2) In Figs. 6c and 7c we have a transition of two cells at the shocks. The ENO flux is used seven times in Fig. 6c, where $\bar{r} = 3$, and 11 times in Fig. 7c, where $\bar{r} = 5$, exactly as predicted by (4.4b).

(3) The efficiency factors in Table V are close to those of Tables 1–2 using the same ε and $\bar{r}$.

(4) The results of the fourth-order MRSENO4 are more accurate than those of the second-order scheme and, accordingly, we use $\bar{r} = 5$ and $\varepsilon = 10^{-5}$; on the other hand, we use the same $\varepsilon_{\text{osc}} = 5 \times 10^{-3}$ in both cases. Note that this last parameter determines the switching between two schemes which have the same order of accuracy; therefore the relatively large value of ε_{osc} does not adversely affect the accuracy in regions of smoothness.

Next we show the results of the second-order MRSENO2 for a Riemann IVP (shock tube) for the Euler equations of compressible gas:

$$w_t + f(w)_x = 0, \quad w(x, 0) = \begin{cases} w_L, & x < 0, \\ w_R, & x > 0, \end{cases} \tag{5.3a}$$

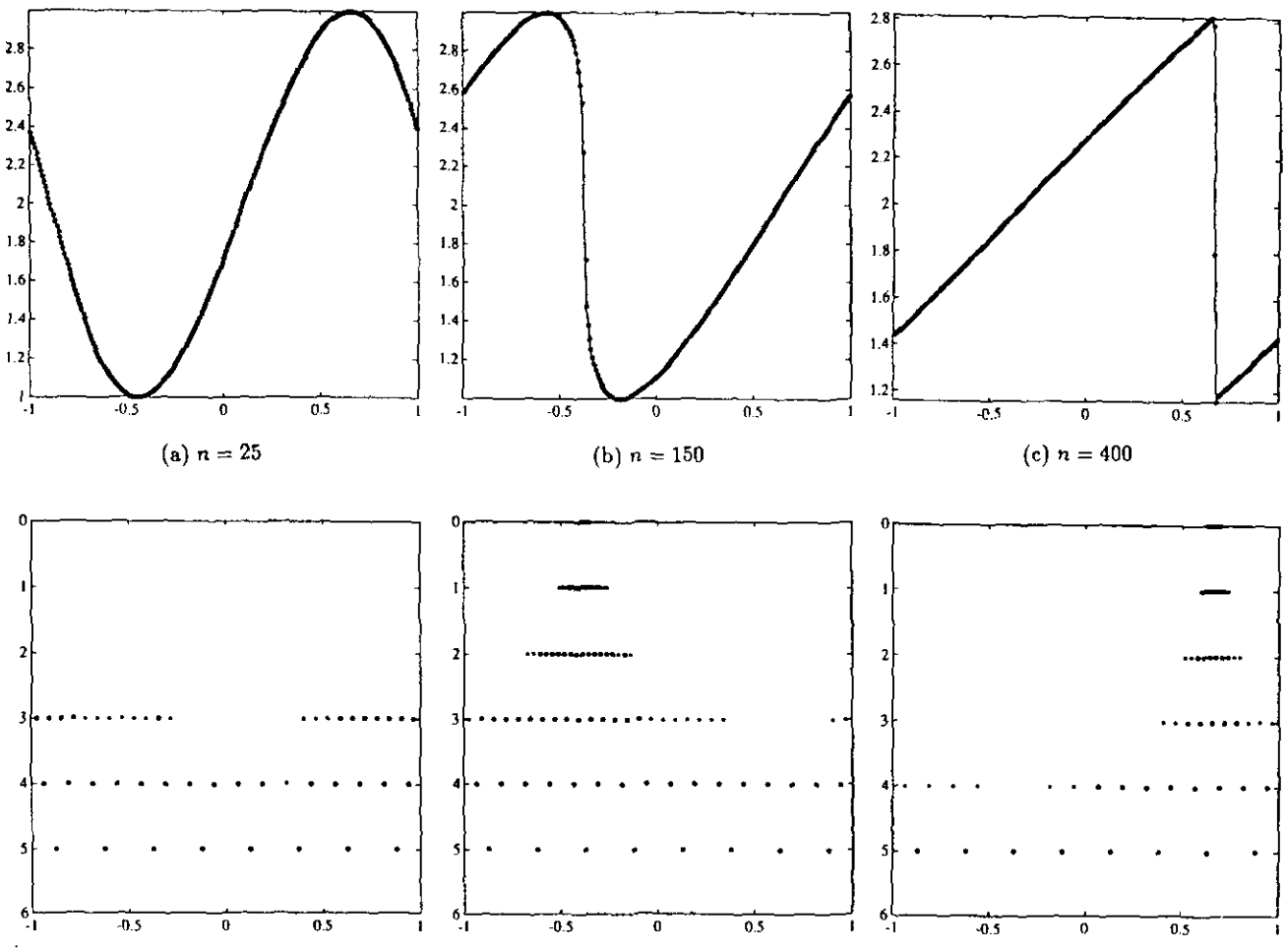

FIG. 7. Fourth-order adaptive multiresolution scheme (MRSENO4).

$$w = (\rho, mE)^T, \quad f(w) = uw + (0, P, Pu)^T, \quad (5.3b)$$

where ρ, m, E are the density, momentum, and energy, respectively; $u = m/\rho$ is the velocity and P is the pressure which is related to w by an equation of state of a polytropic gas with $\gamma = 1.4$,

$$P = (\gamma - 1)(E - \rho u^2/2); \quad (5.3c)$$

the states w_L and w_R in our numerical experiment are those of Sod's shock-tube problem,

$$w_L = (1, 0, 2.5)^T, \quad w_R = (0.125, 0, 0.25)^T. \quad (5.3d)$$

The ENO numerical flux remains the same as in (4.10)–(4.12), except that $f'(w)$ is now the Jacobian matrix $\partial f/\partial w$ and the slopes S_j, S_{j+1} in (4.6b) are computed by the characteristic decomposition

$$S_j = \sum_{q=1}^{3} \overline{m}(l_q \cdot (v_j^n - v_{j-1}^n), \quad l_q(v_{j+1}^n - v_j^n)) \cdot r_q; \quad (5.4)$$

here l_q and r_q are the left-eigenvector (row-vector) and right-eigenvector (column-vector) of the Jacobian matrix $f'(\bar{v})$, where $\bar{v}$ is the Roe-average of v_j^n and v_{j+1}^n (see [1] for more details).

In Fig. 9 and Table VIII we present results of the second-order adaptive multiresolution scheme MRSENO2 for the Riemann IVP (5.1) in $[-1, 1]$ with $N_0 = 512$ and a variable time-step which corresponds to a CFL = 0.8 for the finest grid. We stopped the calculation at $n = 250$ in order to avoid the question of boundary conditions. In Fig. 8 and Table VII we present for the sake of comparison the results of the multiresolution algorithm for the Lax–Wendroff scheme. In both calculations

TABLE IV

SENO4 for Burgers Equation in Fig. 5

IVP	n	ENO calls	E_∞	E_∞ (smooth)	E_1	E_2
(3.1)	150	7	1.49×10^{-2}	1.02×10^{-3}	1.46×10^{-4}	1.13×10^{-3}
	400	7	3.87×10^{-5}	9.30×10^{-6}	2.44×10^{-6}	4.51×10^{-6}
(4.17)	10	15	3.17×10^{-3}	3.17×10^{-3}	3.49×10^{-5}	2.66×10^{-4}
	75	7	4.25×10^{-3}	4.25×10^{-3}	1.06×10^{-4}	4.17×10^{-4}
(4.18)	50	9	5.00×10^{-4}	1.08×10^{-4}	1.20×10^{-5}	5.44×10^{-5}
	100	5	4.65×10^{-6}	4.65×10^{-6}	7.70×10^{-7}	1.18×10^{-6}

Note. $N_0 = 256$, CFL $= 0.8$, $\bar{r} = 3$, $\varepsilon_{\text{osc}} = 5 \times 10^{-3}$.

we used $L = 6$ levels of resolution, $\bar{r} = 3$, $\varepsilon = 5 \times 10^{-4}$, and the definition of $|d_j^k(v^n)|$,

$$|d_j^k(v^n)| = |d_j^k(\rho^n)| + |d_j^k(m^n)| + |d_j^k(E^n)|, \tag{5.5}$$

where the quantities in the RHS of (5.5) are the absolute values of the scalar quantities in (1.7).

In the calculations of MRSENO2 we took $\varepsilon_{\text{osc}} = \varepsilon_1 = \varepsilon/2$; note that from the point of view of algorithm (5.1) this is the most attractive choice, since the two IF statements in (5.1b) can be united into a single one.

In part (a) of each figure we present the multiresolution diagram, where $\mathfrak{D}_\varepsilon(v^n)$ is marked by circles and $\tilde{\mathfrak{D}}^{n+1}$ by asterisks; in Fig. 9a we also mark by asterisks at level 0 the locations in which the ENO flux was used. In parts (b), (c), (d) of each figure we mark by circles the solution of the multiresolution scheme for density, velocity, and pressure, respectively. In Fig. 8 and Table VII we compare these results to the solution of the LW scheme (continuous line) which is computed independently. In Fig. 9 and Table VIII we compare in the same way to the ENO2 scheme. In both Tables VII and VIII we use the definition for E_p, $p = 1, \infty$,

$$E_\infty = \max_{1 \le i \le N_0} \max[e_i(\rho^n), e_i(m^n), e_i(E^n)], \tag{5.6a}$$

$$E_1 = \frac{1}{N_0} \sum_{i=1}^{N_0} [e_i(\rho^n) + e_i(m^n) + e_i(E^n)]/3, \tag{5.6b}$$

where $e_i(\cdot)$ denotes the absolute value of the difference at x_i^0 between the two numerical solutions that are being compared at the corresponding figures.

In Fig. 8 for the Lax–Wendroff scheme we see another "mishap" that can occur due to spurious oscillations combined with a lack of dissipation, namely the creation of a small "negative shock" at $x = 0$. In Fig. 9 we see a solution which is very close to that of ENO2. It is interesting to note that the maximal error in Table VIII occurs at the rarefaction wave and that, if we take a larger value of ε_{osc}, the first spurious oscillations to become noticeable appear to the immediate left of the contact discontinuity. In Table VIII we see that at $n = 50$ about 50% of the computed fluxes are ENO fluxes; at $n = 250$, after separation of the waves only 14% of the computed fluxes are ENO ones. As in the scalar case the two-cell shock requires seven ENO fluxes, the smeared contact-discontinuity requires a little bit more because of its larger spread and that at $n = 250$ only the right corner of the rarefaction requires a "touch of ENO treatment."

6. TOLERANCE PARAMETERS AND CONCLUDING REMARKS

In the following we present analysis of step-function data which suggests that in general $|d_j^1(v^n)|$ at a discontinuity is a good measure for the size of spurious oscillations that could

TABLE V

Second-Order Adaptive Multiresolution Scheme

n	Efficiency μ	ENO/centered	E_∞/E_∞ (smooth)	E_1	E_2
25	4.13	0/62	$7.94 \times 10^{-4}/7.94 \times 10^{-4}$	1.04×10^{-4}	1.51×10^{-4}
150	3.56	7/65	$7.19 \times 10^{-2}/4.48 \times 10^{-3}$	9.93×10^{-4}	5.61×10^{-3}
400	5.69	7/38	$1.32 \times 10^{-2}/7.58 \times 10^{-4}$	1.54×10^{-4}	8.54×10^{-4}

Note. $N_0 = 256$, CFL $= 0.8$, $\bar{r} = 3$, $L = 5$, $\varepsilon = 10^{-3}$, $\varepsilon_{\text{osc}} = 5 \times 10^{-3}$.

TABLE VI

Fourth-Order Adaptive Multiresolution Scheme

n	Efficiency μ	ENO/centered	E_∞/E_∞ (smooth)	E_1	E_2
25	4.74	0/54	$1.32 \times 10^{-5}/1.32 \times 10^{-5}$	2.88×10^{-6}	3.86×10^{-6}
150	2.81	9/82	$1.78 \times 10^{-2}/7.63 \times 10^{-4}$	1.94×10^{-4}	1.47×10^{-3}
400	4.27	11/48	$8.64 \times 10^{-5}/1.50 \times 10^{-5}$	4.35×10^{-6}	8.73×10^{-6}

Note. $N_0 = 256$, CFL = 0.8, $\bar{r} = 5$, $L = 5$, $\varepsilon = 10^{-5}$, $\varepsilon_{\text{osc}} = 5 \times 10^{-3}$.

be generated there by a centered scheme. The approximation (1.7a) by which we get our prediction $\bar{u}_j^0$ is a centered one and thus generates spurious oscillations at a jump discontinuity. Let $u_d(x)$ be the step function

$$u_d(x) = \begin{cases} u_L, & x \le j_d \cdot h_0, \\ u_R, & x > j_d \cdot h_0, \end{cases} \tag{6.1a}$$

for which the cell-averages on the finest grid are

$$\bar{u}_j^0 = \begin{cases} u_L, & j \le j_d, \\ u_R, & j \ge j_d + 1, \end{cases} \tag{6.1b}$$

and let $[u] = u_R - u_L$ denote the jump in (6.1). Applying (1.7) to (6.1b) we get that for $s = 1$, the nonzero coefficients $d_j^1(\bar{u}^0)$ are

$$d_{j_0-1}^1 = d_{j_0}^1 = -0.1250[u], \quad \text{if } j_d = 2j_0 \tag{6.2a}$$

or

$$d_{j_0}^1 = 0.3750[u], \quad d_{j_0-1}^1 = d_{j_0+1}^1 = -0.0625[u], \quad \text{if } j_d = 2j_0 + 1, \tag{6.2b}$$

and for $s = 2$ we get

$$d_{j_0-1}^1 = d_{j_0}^1 = -0.1484[u], \tag{6.3a}$$

$$d_{j_0-2}^1 = d_{j_0+1}^1 = 0.0234[u], \quad \text{if } j_d = 2j_0$$

or

$$\begin{aligned} &d_{j_0}^1 = 0.3516[u], \quad d_{j_0-1}^1 = d_{j_0+1}^1 = -0.0578[u], \\ &d_{j_0-2}^1 = d_{j_0-2}^1 = d_{j_0+2}^1 = 0.0117[u], \quad \text{if } j_d = 2j_0 + 1. \end{aligned} \tag{6.3b}$$

We observe that if $[u]$ is such that $|d_j^1| \le \varepsilon_1$, then d_j^1 is set to zero by the truncation operator (1.12), and thus the decoded value $\hat{u}_j^0$ is obtained from $\bar{u}^1$ by the central approximation (1.7a); this may introduce spurious oscillations of the type (6.2)–(6.3) which are bounded by the tolerance ε. Note that if the approximation would generate spurious oscillations which are larger than $\varepsilon_1 = \varepsilon/2$, then the corresponding d_j^1 is kept in order to correct the predicted value and thus the original step-data is recovered exactly. In the multiresolution scheme (2.3), (2.6) if $|d_j^1| \le \varepsilon_1$ then the numerical flux, which is a discontinuous function of x for a moving shock, is interpolated from the coarser grid by the central approximation in (2.6); this may likewise introduce spurious oscillations which are at most $O(\varepsilon)$ (see (2.5)). If, on the other hand, the shock is large, then we use the exact numerical flux function, which amounts to locally using the given fine-grid scheme.

We turn now to consider the case where the fine-grid scheme which is used at the shock is the centered one in (4.14). It is well known that centered schemes which attain the maximal order of accuracy for the stencil are interpolatory in the constant coefficient case

TABLE VII

Multiresolution Lax–Wendroff Scheme for Gasdynamics

n	Efficiency μ	E_∞	E_1
50	5.75	6.97×10^{-4}	1.44×10^{-5}
100	4.03	1.91×10^{-3}	4.74×10^{-5}
150	3.53	7.90×10^{-3}	1.00×10^{-4}
200	3.44	6.33×10^{-3}	1.40×10^{-4}
250	3.22	1.04×10^{-2}	2.05×10^{-4}

Note. $N_0 = 512$, CFL = 0.8, $\bar{r} = 3$, $L = 6$, $\varepsilon = 5 \times 10^{-4}$.

TABLE VIII

Second-Order Adaptive Multiresolution Scheme for Gasdynamics

n	Efficiency μ	ENO/centered	E_∞	E_1
50	4.97	50/53	1.27×10^{-3}	1.46×10^{-5}
100	4.06	39/87	2.55×10^{-3}	5.38×10^{-5}
150	3.68	28/111	2.11×10^{-3}	8.44×10^{-5}
200	3.61	23/119	1.97×10^{-3}	1.08×10^{-4}
250	3.44	21/128	1.98×10^{-3}	1.29×10^{-4}

Note. $N_0 = 512$, CFL = 0.8, $\bar{r} = 3$, $L = 6$, $\varepsilon = 5 \times 10^{-4}$, $\varepsilon_{\text{osc}} = 2.5 \times 10^{-4}$.

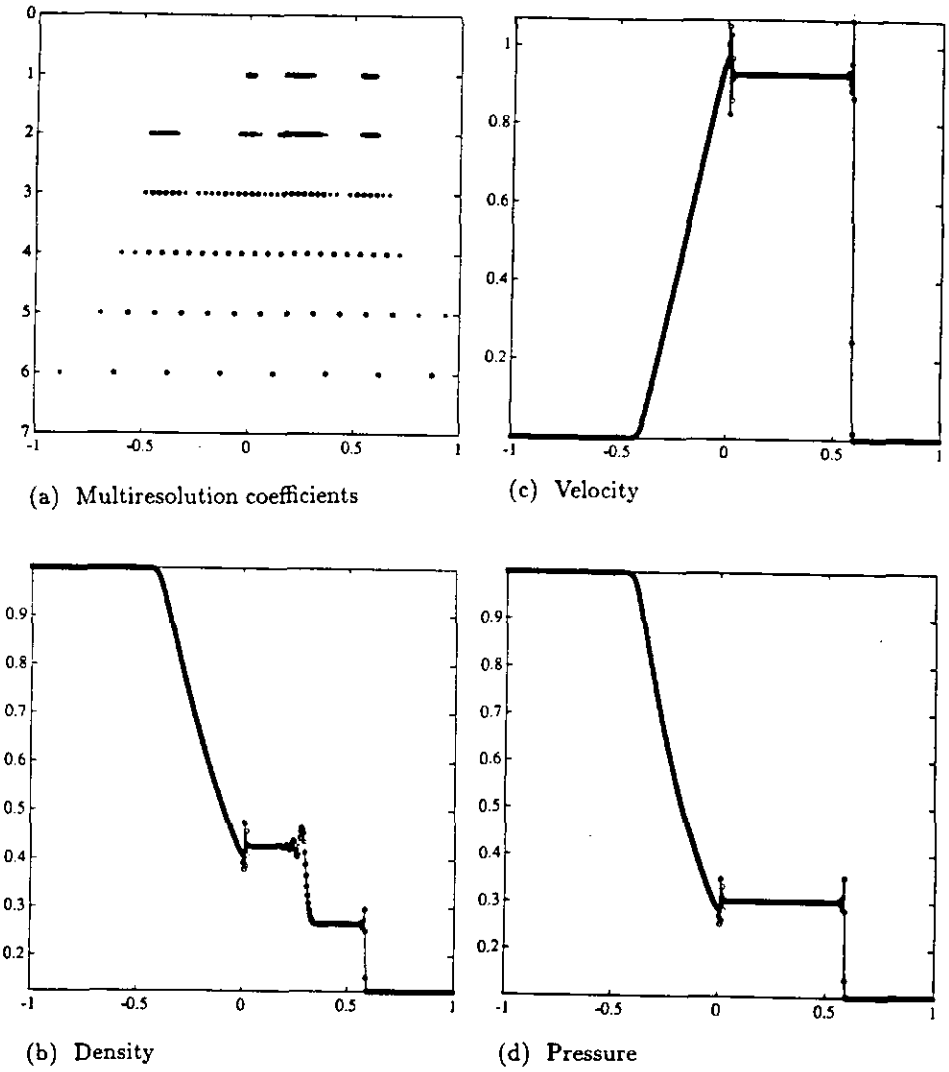

FIG. 8. Multiresolution LW scheme for gasdynamics.

$$w_t + aw_x = 0, \quad a = \text{const.}, \tag{6.4a}$$

i.e.,

$$v_j^{n+1} = Q_{j,s}(x_j^0 - a\tau; v^n), \tag{6.4b}$$

where $Q_{j,s}$ is the unique polynomial of degree $r = 2s$ for which

$$Q_{j,s}(x_{j-l}^0; v^n) = v_{j-l}^n, \quad |l| \le s. \tag{6.4c}$$

When applied to the step-function data (6.1b) we find that the maximal spurious oscillation Δ_j at the cell $[x_{j-1}^0, x_j^0]$ that can be introduced by the centered interpolation $Q_{j,s}$ is

$$\Delta_{j_d} = \Delta_{j_d+1} = -0.1250[u] \quad \text{for } s = 1\ (r = 2), \tag{6.5a}$$

$$\Delta_{j_d} = -\Delta_{j_d+1} = -0.1336[u], \tag{6.5b}$$

$$\Delta_{j_d-1} = -\Delta_{j_d+2} = 0.0234[u] \quad \text{for } s = 2\ (r = 4). \tag{6.5c}$$

The comparison between the values of d_j^l for a jump-discontinuity (6.2)–(6.3) and the size of spurious oscillations (6.5) that can be generated by a centered scheme in the same situation for the constant-coefficient case shows that the maximal value of $|d_j^l|$ at a discontinuity can serve as an upper bound for the largest spurious oscillation that would be generated by the centered scheme if it were used there.

Thus, given a discontinuity with jump $[u]$ we can describe the solution of SENO there as follows: If the maximal value of $|d_j^l|$ in (6.2)–(6.3) is larger than ε_{osc}, then SENO uses the ENO flux at the gridpoints calculated by algorithm (4.2); it is easy to see that the switching prescribed by this algorithm is sufficient to ensure a nonoscillatory solution for both SENO2 and SENO4. If, on the other hand, the maximal $|d_j^l|$ is less than

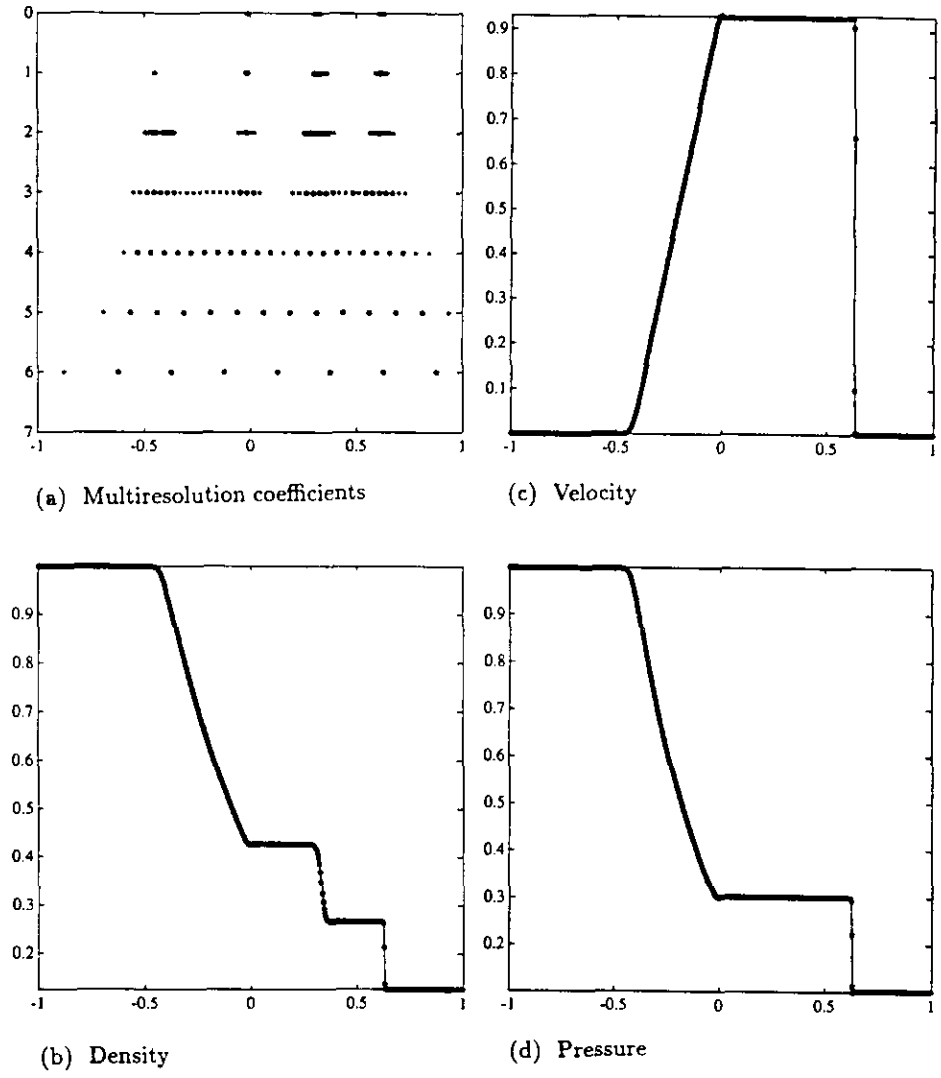

FIG. 9. Second-order adaptive multiresolution scheme (MRSENO2) for gas dynamics.

ε_{osc}, then the oscillatory centered scheme will be used at this discontinuity, but then the above analysis indicates that the size of the spurious oscillations will also be smaller than ε_{osc}.

We remark that at first glance it seems that for $r = 4$ we have to switch to an ENO flux at the larger stencil $\{x_{2j-1-l}\}$, $|l| \leq 2$, but a closer examination of (6.2b) and (6.3b) shows that even with the smaller stencil of (4.2), the flux $\bar{f}^{\text{CTR}}$ is used with data that does not contain a discontinuity; this is confirmed by the numerical results in Figs. 5 and 7.

From the above analysis it is clear that a choice of $\varepsilon_{\text{osc}} \ll \varepsilon$ is not computationally reasonable since the expensive ENO flux will be used to avoid $O(\varepsilon_{\text{osc}})$ oscillations, while larger $O(\varepsilon)$ oscillations may be introduced by the data compression part of the algorithm. The choice $\varepsilon_{\text{osc}} \gg \varepsilon$ can be used to reduce the number of ENO flux calls at the risk of generating $O(\varepsilon_{\text{osc}})$ spurious oscillations, if the user considers them to be acceptable in the particular application.

In general we suggest choosing

$$\varepsilon_{\text{osc}} = \varepsilon_1 = \varepsilon/2 \tag{6.6}$$

(as we did in Fig. 9) and taking ε to be of the size of the local truncation error of the centered scheme in the smooth part of the solution. In [2] we showed that the data-compression error accumulates in the same way as the local truncation error of the fine-grid scheme. Hence if we choose ε to be of the same order as the local truncation error we get that the multiresolution results are of the same quality as those of the fine-grid calculation. Taking ε_{osc} to be of the order of the local truncation error makes the adaptive scheme conceptually similar to the global ENO schemes, where spurious oscillations are possible only on the level of local truncation error. The choice (6.6) is particularly attractive since it saves an IF statement in (5.1b). The

resulting adaptive multiresolution scheme produces results which are somewhat superior to those of the global ENO scheme (because of the better performance of the centered scheme in the smooth part of the solution) at a reduced computational cost which is obtained by interpolating fluxes from the coarsest grid for which the solution is locally well resolved and by using the expensive ENO flux calculation only in the immediate neighborhood of irregularities in the solution.

We remark that the analysis in (6.2)–(6.5) which shows that $|d_j^l|$ dominates the size of spurious oscillations in the centered scheme is based on the *scalar* constant coefficient case; thus it should be extended to a system of conservation laws through locally defined characteristic variables. Thus the norm $|d_j^k|$ should be defined as a standard norm for the vector

$$(l_1 \cdot d_j^k, ..., l_q \cdot d_j^k) \tag{6.7a}$$

such as

$$|d_j^k|_1 = \sum_{m=1}^{q} |l_m \cdot d_j^k|, \tag{6.7b}$$

where l_m are the left-eigenvectors of $f'(v_j^k)$. We observe that unlike (5.5), the definition (6.7b) is dimensionally correct but more expensive to compute. The use of the dimensionally incorrect (but equivalent) norm in (5.5) may force us into taking ε and ε_{osc} which are smaller than what is actually needed to achieve our computational goal.

Finally we point out that in situations where $|d_j^l| > \varepsilon_{\text{osc}}$ only at shocks, it does make sense to use an adaptive scheme with a second-order ENO scheme for the shocks and a higher-order centered scheme for the smooth part of the solution.

ACKNOWLEDGMENT

This research was supported by Grants ONR-N00014-92-J-1890 and NSF-DMS91-03104.

REFERENCES

1. E. Bacry, S. Mallet, and G. Papanicolau, *Math. Modelling Numer. Anal.* **26,** 703 (1992).
2. P. Colella and P. R. Woodward, *J. Comput. Phys.* **54,** 174 (1984).
3. I. Daubechies, *Commun. Pure Appl. Math.* **41,** 909 (1988).
4. A. Harten, ICASE Report 91-77, September 1991; in *Proceedings, ICASE/LaRC Workshop on Algorithmic Trends in CFD for the 90's.*
5. A. Harten, *J. Appl. Numer. Math.* **12,** 153 (1993); UCLA CAM Report 92-08, February 1992.
6. A. Harten, UCLA CAM Report 93-03, March 1993; *Commun. Pure Appl. Math.*, to appear.
7. A. Harten and I. Yad-Shalom, ICASE Report 92-55, October 1992; *SIAM J. Numer. Anal.*, **31,** 1191 (1994).
8. A. Harten, B. Engquist, S. Osher, and S. R. Chakravarthy, *J. Comput. Phys.* **71,** 231 (1987).
9. B. van Leer, *J. Comput. Phys.* **32,** 101 (1979).
10. J. Liandrat and Ph. Tchamitchian, ICASE Report 90-83, December 1990 (unpublished).
11. Y. Maday and J. C. Ravel, Tech. Report, Université Pierre et Marie Curie, Lab. D'Analyse Numérique, January 1992 (unpublished).